CDDpress

www.nature.com/cddis

ARTICLE OPEN

NSUN2 mediates intestinal stem cell expansion and colorectal tumour initiation via MAPK/ERK signalling

Aslihan Bastem Akan[1,2], Caroline V. Billard[1,2], Szu-Ying Chen[3], Po-Hsien Huang[3], Patrizia Cammareri[1,2], Vidya Rajasekaran[1,2], Adam E. Hall[1,2,4], Paula Preyzner[1,2], Sebastian Öther-Gee Pohl[1,2], Susan M. Farrington[1,2], Malcolm G. Dunlop[1,2], Farhat V. N. Din[1,2] and Kevin B. Myant[1,2]✉

Colorectal cancer is initiated by loss of *APC*, which drives expansion of LGR5+ intestinal stem cell (ISC) populations. Whilst LGR5 + ISC expansion is a critical step for tumour initiation and progression, its regulation is poorly understood. Emerging evidence suggests post-transcriptional RNA modifications play a key role in cancer biology, but their role in CRC initiation has not been explored. Here, we identify the m^5C methyltransferase NSUN2 as a key regulator of ISC expansion and intestinal tumourigenesis. NSUN2 is upregulated in multiple CRC mouse models and human tumours, and its depletion impairs ISC expansion and hyperproliferation, leading to reduced tumour initiation. Transcriptome-wide bisulfite sequencing revealed that NSUN2 mediates m^5C methylation on mRNAs encoding key ISC regulators and components of the MAPK/ERK pathway. Mechanistically, loss of NSUN2 reduces ERK phosphorylation in *Apc*-deficient models, and oncogenic $Kras^{G12D}$ expression is sufficient to restore ERK signalling and rescue ISC expansion. Together, this establishes a novel role for NSUN2 as a key regulator of ISC-driven CRC initiation and describes a critical molecular mechanism linking m^5C methylation to MAPK-driven stem cell transformation.

Cell Death and Disease (2026)17:322 ; https://doi.org/10.1038/s41419-026-08560-0

INTRODUCTION

Colorectal cancer (CRC) is the third most common cancer worldwide, with nearly two million new cases annually, and the second most common cause of cancer-related death [1]. CRC initiation is driven by malignant transformation of LGR5+ intestinal stem cells (ISCs), which maintain normal intestinal homoeostasis through constant self-renewal and differentiation [2, 3]. This process is normally tightly controlled by signalling pathways such as WNT, MAPK, BMP and TGF-β. However, during tumourigenesis, these pathways become dysregulated, leading to ISC expansion and tumour formation [4]. Most CRCs are initiated by loss of the *APC* gene, leading to a hyper-proliferative early stage, and progress to metastatic carcinoma via accumulation of additional mutations in genes, including *TP53*, *KRAS* and *SMAD4* [5–9]. Although targeted therapies and immunotherapies have improved outcomes for some patients, CRC remains difficult to treat due to therapy resistance and disease relapse [10–12]. This is often driven by the activity of cancer stem cells, a subpopulation of tumour-initiating cells which arise from transformed ISCs via aberrant genetic or epigenetic pathways and which sustain tumour growth and evade conventional treatments [13–16].

Post-translational modifications of RNA are important regulators of tumourigenesis. These modifications are found in distinct RNA types and influence a multitude of diverse functions, such as gene expression, RNA stability, RNA localisation and protein translation [17–22]. Over 170 RNA modifications that control the fate of RNA and mediate cellular functions have been identified [23]. Of these, 5-methylcytidine (m^5C) is one of the best described and was first discovered by Amos and Korn [24]. m^5C is widely found in tRNAs and rRNAs, where it stabilises RNA structure and regulates translation efficiency. More recently, m^5C has been identified in mRNA, where it modulates RNA stability [25–27], export [28] and translation [18]. RNA modifications are regulated by diverse proteins categorised as writers, readers and erasers [29]. m^5C can be introduced to RNAs by the NSUN family of proteins (NSUN1 to NSUN7) or DNMT2 [30], NSUN2 and NSUN6 have been shown to modulate mRNA methylation [30–32]. Of the NSUN proteins, NSUN2 has gained increasing attention due to its oncogenic potential.

NSUN2 was first identified as a target of the well-known proto-oncogene MYC in the epidermis [33, 34]. It catalyses m^5C methylation in tRNAs, rRNAs and described more recently, mRNAs [25, 35–44]. NSUN2-mediated m^5C has been shown to regulate RNA stability, translation efficiency and cellular differentiation. Multiple research groups have reported increased NSUN2 mRNA and protein expression in various cancers, including gastric, oesophageal, hepatocellular, bladder, osteosarcoma, and cervical cancers. Additionally, NSUN2 has been demonstrated to play a role in regulating tumour growth, migration, and invasion [26, 45–49]. However, the role of NSUN2, and that of mRNA m^5C

[1]Institute of Genetics and Cancer, The University of Edinburgh, Western General Hospital Campus, Edinburgh, UK. [2]Cancer Research UK Scotland Centre, Institute of Genetics and Cancer, The University of Edinburgh, Western General Hospital, Edinburgh, UK. [3]Institute of Basic Medical Sciences, National Cheng Kung University, Tainan City, Taiwan. [4]Present address: Wellcome Sanger Institute, Wellcome Genome Campus, Cambridge, UK. ✉email: kevin.myant@ed.ac.uk

Edited by Professor Gennaro Ciliberto

Received: 29 May 2025 Revised: 26 January 2026 Accepted: 6 March 2026
Published online: 19 March 2026

methylation, in intestinal homoeostasis and colorectal tumourigenesis remains poorly understood. Therefore, a better understanding of the role of m^5C mRNA methylation and its role in ISC expansion and tumour initiation is crucial for fully defining the mechanisms mediating tumour initiation.

In this study, we define the role of NSUN2 in CRC initiation using *Apc*-deficient CRC mouse models. We find that NSUN2 is overexpressed following *Apc*-loss. Moreover, high expression of *NSUN2* in human CRC correlates with poor disease outcome. Functionally, we find that NSUN2 depletion impairs ISC-driven hyperproliferation and cancer stemness in *Apc*-deficient in vitro organoids and in vivo cancer models, without affecting normal intestinal homoeostasis. Transcriptome-wide bisulfite analysis reveals that loss of NSUN2 leads to bidirectional changes in m^5C mRNA methylation, particularly in mRNAs encoding ISC regulators and MAPK/ERK components. Furthermore, we find that MAPK/ERK pathway activation in *Apc*-deficient organoids depends on NSUN2 expression, an effect rescued by expression of oncogenic $Kras^{G12D}$. Together, these findings establish NSUN2-mediated m^5C methylation as a crucial regulator of ISC expansion and CRC initiation, for the first-time linking RNA modifications to colorectal stem cell transformation.

RESULTS

NSUN2 is upregulated in *Apc-loss-driven* hyper-proliferative intestine

To better understand the role of m^5C methylation in Wnt-driven tumour initiation, we analysed our previously generated RNA-seq dataset derived from intestinal epithelium of *Vil-CreERT2* $Apc^{fl/fl}$ mice following tamoxifen-induced *Apc* deletion [50]. This analysis revealed significant overexpression of the m^5C methyltransferase *Nsun2*, but not other known RNA m^5C methyltransferases, readers or eraser enzymes, following *Apc* loss and Wnt signalling activation (Supplementary Fig. S1C and D). To further characterise NSUN2 expression in colorectal tumourigenesis, we performed IHC staining (Fig. 1A and B) and WB (Fig. 1C, D and Supplementary Fig. S1D, E) for NSUN2 in normal and *Apc*-deficient mouse intestines, which indicated elevated NSUN2 expression in hyper-proliferative intestines, validated by β-CATENIN levels in Supplementary Fig. S1A, B. We further analysed *Nsun2* expression in normal intestinal tissue, finding elevated expression of *Nsun2* in ISCs sorted on the basis of EPHB2 expression [51] (Supplementary Fig. S1F). We next investigated NSUN2 expression in intestinal adenomas and found increased NSUN2 expression in adenomas arising in the colon from the spontaneous *VilCreERT2-Apc*$^{+/-}$ model (Fig. 1E and F) [52]. To analyse NSUN2 expression following malignant stem cell transformation, we used the tamoxifen-inducible *Lgr5-IRES-eGFP-CreERT2* $Apc^{fl/fl}$ model where both copies of *Apc* are deleted in *Lgr5*+ stem cells [4]. Again, NSUN2 expression was elevated in adenomas arising from Wnt hyperactivation in stem cells (Fig. 1G and H). Together, these data demonstrate elevated expression of NSUN2 in *Apc*-deficient CRC models, suggesting a potential role in tumourigenesis.

NSUN2 is overexpressed in human CRC and high expression of NSUN2 correlates with poor prognosis

Next, we utilised The Cancer Genome Atlas Colon (TCGA-COAD) and Rectum Adenocarcinoma (TCGA-READ) datasets in order to investigate the expression of NSUN2 in colorectal cancer patients. In TCGA-COAD patients, NSUN2 is higher in primary colon tumour samples compared to normal colon (Fig. 2A; $p < 0.0001$) and correlates with poor overall (Fig. 2B; $p = 0.035$) and relapse-free survival (Fig. 2C; $p = 0.007$). Similar NSUN2 expression and survival correlations were observed in TCGA-READ patients, except for overall survival (Fig. 2D–F). Given that *APC, KRAS* and *P53* are key drivers in the 'adenoma-to-carcinoma' sequence model of CRC, we next analysed *NSUN2* expression in relation to these mutations [6]. We analysed *NSUN2* expression in patients of TCGA-COAD and TCGA-READ datasets in the case of mutant and wild-type versions of these major driver genes. The results showed that *NSUN2* is overexpressed in patients bearing *APC*-truncation (left, $p = 0.0017$, $n = 139$ vs. 385) and *KRAS*-mutation (middle, $p = 0.0011$, $n = 308$ vs. 212), but is not significantly associated with *P53*-mutation (right, $p = 0.0717$, $n = 211$ vs. 309) (Supplementary Fig. S2A). We also investigated the expression of *NSUN2* according to cancer stage but found no differences (Supplementary Fig. S2B and C). Altogether, these findings indicate that *NSUN2* expression is increased in colorectal cancer and high expression correlates with poor prognosis.

Nsun2 depletion reduces self-renewal of $Apc^{fl/fl}$ 3D mouse organoids

To evaluate whether NSUN2 is required for tumourigenic growth, we knocked down its expression in $Apc^{fl/fl}$ organoids using shRNA. We transduced $Apc^{fl/fl}$ organoids with control and two independent sh*Nsun2*-targeting lentiviral particles; hereafter named shCtrl, shNsun2-1 and shNsun2-2, respectively. RNA and protein analysis demonstrated effective knockdown of NSUN2 in this organoid model (Fig. 3A, B and Supplementary Fig. S3A). Dot blot analysis showed this silencing of *Nsun2* resulted in a functional reduction of global RNA m^5C methylation in $Apc^{fl/fl}$ organoids (Fig. 3C and D). To determine the phenotypic effects of *Nsun2* and RNA m^5C methylation depletion on organoid growth, we carried out colony formation assays. The ability of $Apc^{fl/fl}$ single cells to form organoids was significantly decreased following *Nsun2*-depletion (Fig. 3E and F). In addition to clonogenic capacity, organoid size and overall cell viability measured by Resazurin assay [53] were reduced in $Apc^{shNsun2}$ organoids (Fig. 3G and H). Since clonogenic capacity is highly related to self-renewal capacity and stem cell activity, we examined mRNA expression of stem cell marker genes in *Nsun2*-depleted $Apc^{fl/fl}$ organoids. Several well-characterised intestinal stem cell markers, such as *Lgr5, Ascl2, Igfbp4, Lrig1*, and *Smoc2*, were significantly decreased following *Nsun2* depletion, indicative of a loss of stem cell capacity (Fig. 3I). Thus, *Nsun2* is essential for maintaining cancer stem cell function in a Wnt-driven CRC organoid model, potentially through its role in m^5C methylation.

Nsun2 is required for *Apc*-loss-mediated hyper-proliferation and stem cell expansion in vivo

To investigate this in a more physiological context, we next determined the role of NSUN2 in normal intestinal homoeostasis and *Apc*-loss-induced hyper-proliferation. To do this, we generated *Vil-CreERT2* $Nsun2^{fl/fl}$ (*Nsun2*), and *Vil-CreERT2-*$Apc^{fl/fl}$ $Nsun2^{fl/fl}$ (*Apc Nsun2*) mice by crossing to *Vil-CreERT2-Wt* (*Wt*) and -$Apc^{fl/fl}$ (*Apc*) lines [54] (Fig. 4A). Mice were induced with tamoxifen, intestinal crypts isolated 4 days post induction, and *Nsun2* knockout validated at mRNA and protein levels (Fig. 4B and C). Immunohistochemistry staining also demonstrated effective deletion of NSUN2 in *Nsun2* and *Apc Nsun2* intestines (Fig. 4D, bottom). Histological analysis of intestines revealed a reduction in *Apc*-loss driven hyperproliferation following *Nsun2* deletion with a significantly reduced number of $BrdU^{+ve}$ proliferative cells in *Apc Nsun2* intestines compared to *Apc* (Fig. 4D middle and Fig. 4E). Additionally, expression of ISC markers, such as *Lgr5*, *Ascl2*, *Smoc2* and *Lrig1* was substantially diminished in *Apc Nsun2* intestines (Fig. 4F, Supplementary Fig. S4A) consistent with our findings in in *Nsun2*-depleted $Apc^{fl/fl}$ organoids (Fig. 3). To confirm these findings, we carried out RNAscope for the ISC marker *Lgr5*. We found a robust induction of expression following *Apc* deletion, consistent with previous reports of Wnt-driven stem cell expansion (Fig. 4G and Supplementary Fig. S4B, C). Deletion of *Nsun2* partially abrogated the increase in *Lgr5*, suggesting it is required for stem cell expansion following *Apc* deletion (Fig. 4G and Supplementary Fig. S4B, C). To further validate the stem cell loss

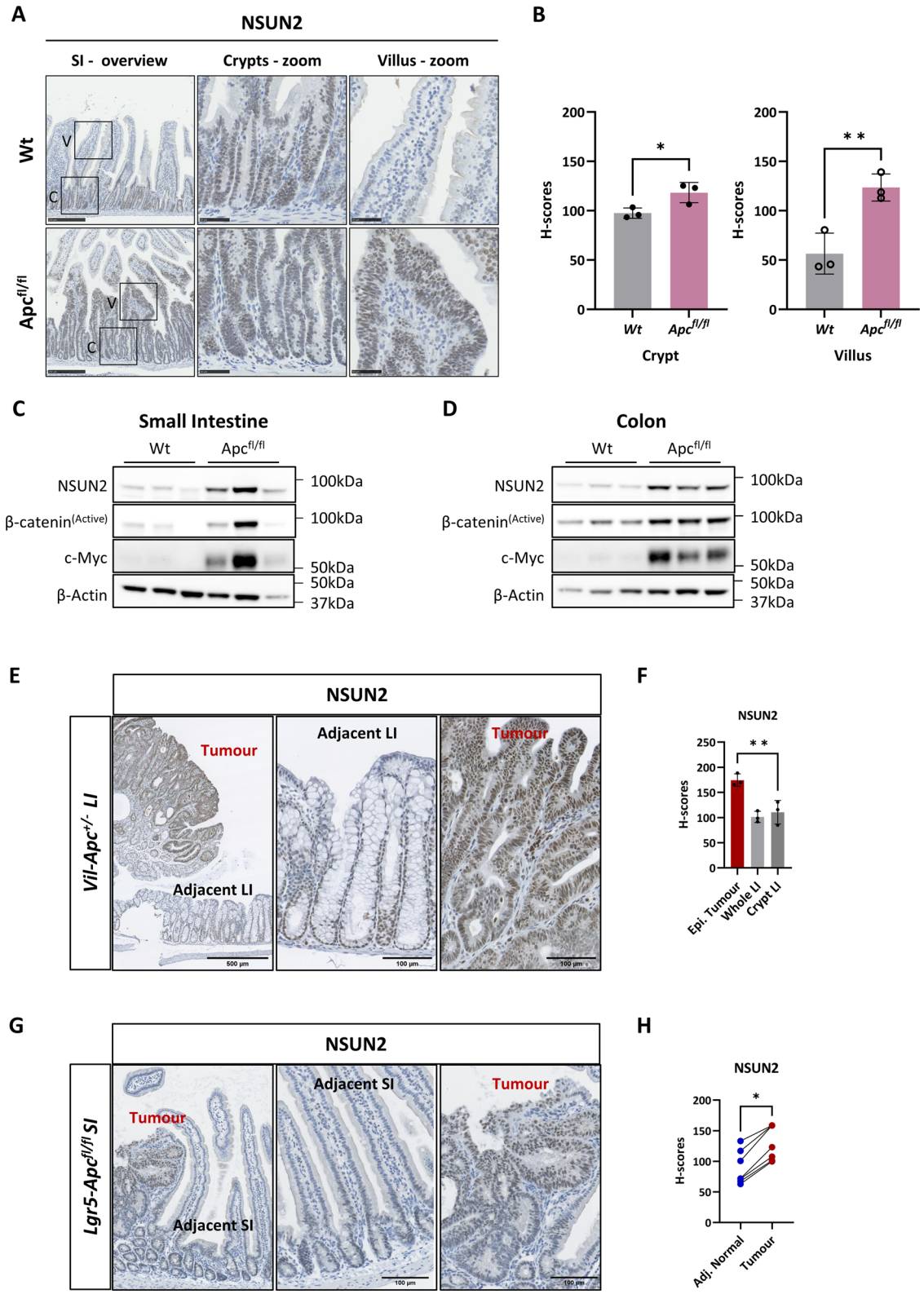

phenotype, we cultured single intestinal cells from *Apc* and *Apc Nsun2* intestines ex vivo. Cells isolated from *Apc Nsun2* intestines had reduced clonogenic capacity, indicative of reduced stem cell function (Supplementary Fig. S4D–F).

To determine whether NSUN2 is required for normal tissue homoeostasis, we next investigated the effects of *Nsun2*-loss on the normal intestine both at phenotypic and transcriptomic levels. Despite robust *Nsun2* deletion in *Nsun2* mice (Fig. 4B and C), ISC gene expression was unchanged compared to *Wt* control mice (Fig. 4F, G, Supplementary Fig. S4A–C). Moreover, loss of *Nsun2* did not affect normal intestinal histology or proliferation (Fig. 4D and E). Together, these findings show that while *Nsun2* is dispensable

Fig. 1 RNA 5-methylcytidine writer, NSUN2, is upregulated following *Apc-loss in* mouse small and large intestinal tissues. **A** Representative images of NSUN2 expression in wild-type and $Apc^{fl/fl}$ small intestinal tissues using immunohistochemistry method. C represents crypt and V represents villus. Scale bars are shown as 500 µm (overview) and 100 µm (magnified). **B** Histo-score quantification of NSUN2 expression using immunohistochemistry method in wild-type and $Apc^{fl/fl}$ small intestinal tissues (data are presented as mean ± SD; $*p = 0.0356$, $**p = 0.0096$; two-tailed *t*-test, $n = 3$ vs. 3 biologically independent mice). **C** Images of western blotting analysis for NSUN2, Active β-Catenin, c-Myc and a house-keeping control β-ACTIN protein expressions in wild-type and $Apc^{fl/fl}$ mouse small intestines. **D** Images of western blotting analysis for NSUN2, Active β-Catenin, c-Myc and a house-keeping control β-ACTIN protein expressions in wild-type and $Apc^{fl/fl}$ mouse colons. **E** Representative immunohistochemistry images of NSUN2 expression in normal adjacent tissue and tumours tissue from Vil-CreERT2-$Apc^{+/-}$ mouse colon. **F** Histo-score quantification of (**E**). Data are presented as mean ± SD; $**p = 0.0058$. Ordinary one-way ANOVA test compared to the epithelial tumour, $n = 3$ biologically independent mice. **G** Representative immunohistochemistry images of NSUN2 expression in normal adjacent tissue and tumour tissue from Lgr5-IRES-eGFP-CreERT2-$Apc^{fl/fl}$ mouse small intestines. **H** Histo-score quantification of (**G**). Data are presented as mean ± SD; $*p = 0.0189$; two-tailed *t*-test, $n = 7$ adjacent normal tissue vs. $n = 7$ tumour tissue parts used from $n = 3$ biologically independent mice.

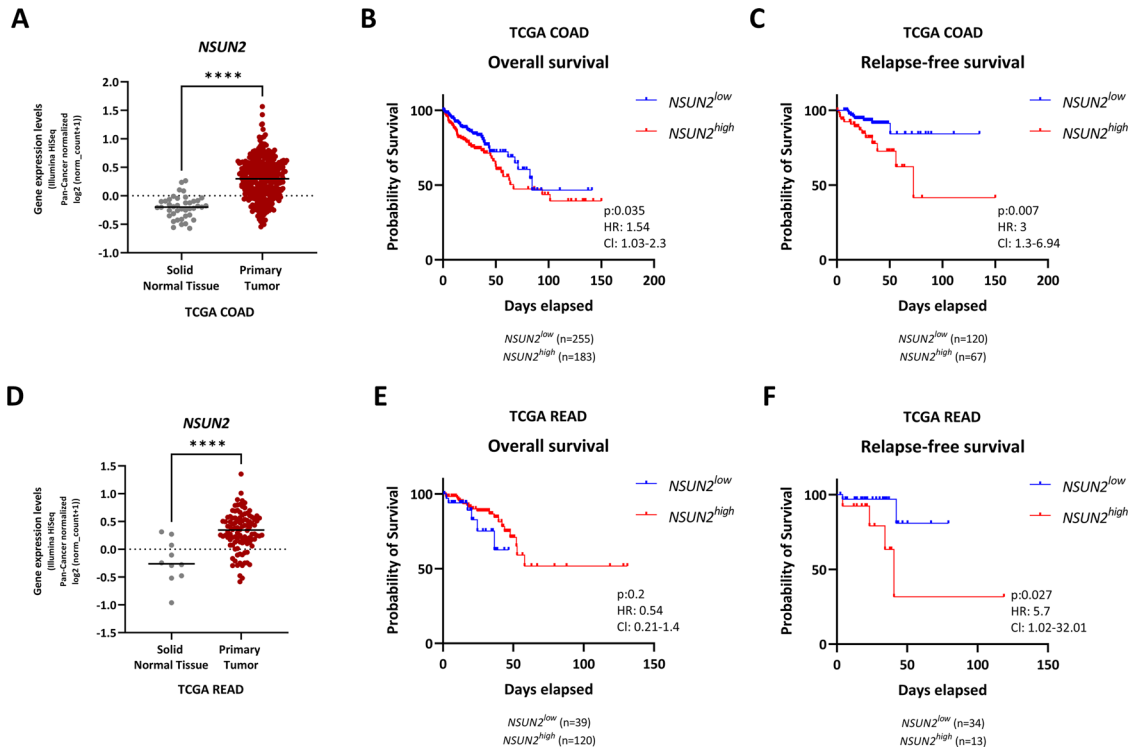

Fig. 2 NSUN2 is overexpressed in the patient's primary tumour compared to adjacent normal tissue and high NSUN2 correlated with poor survival. **A** *NSUN2* mRNA expression is detected in primary tumours of TCGA COAD patients compared to normal adjacent tissues (NAT) in the Xenabrowser platform [69]. log2(normalised_count + 1) gene expression levels are represented by Illumina HiSeq. *z*-scores represent normalised gene expression in tumour samples over a reference (normal) sample (data are presented as mean ± SD; $****p < 0.0001$; two-tailed *t*-test, $n = 41$ normal adjacent tissue vs. $n = 325$ primary tumour). **B** and **C** Overall survival and relapse-free survival of patients in the TCGA COAD dataset based on NSUN2 expression. Overall and relapse-free survival of human CRC patients separated by high vs. low/intermediate *NSUN2* expression. The red line represents $NSUN2^{high}$ and the blue line represents $NSUN2^{low}$ patients. Log-rank *P* value, hazard ratio (HR) and 95% confidence intervals (CI) presented. **D** *NSUN2* mRNA expression is detected in primary tumours of TCGA READ patients compared to normal adjacent tissues (NAT) in the Xenabrowser platform [69]. log2(normalised_count+1) gene expression levels are represented by Illumina HiSeq. *z*-scores represent normalised gene expression in tumour samples over a reference (normal) sample (data are presented as mean ± SD; $****p < 0.0001$; two-tailed *t*-test, $n = 10$ normal adjacent tissue vs. $n = 104$ primary tumour). **E** and **F** Overall survival and relapse-free survival of patients in the TCGA READ dataset based on NSUN2 expression. Overall and relapse-free survival of human CRC patients separated by high vs. low/intermediate *NSUN2* expression. The red line represents $NSUN2^{high}$ and the blue line represents $NSUN2^{low}$ patients. Log-rank *P* value, hazard ratio (HR), and 95% confidence intervals (CI) are presented.

for normal intestinal homoeostasis, it is critical for sustaining *Apc*-loss-driven stem cell expansion and hyperproliferation.

Loss of *Nsun2* in *Apc*-deficient intestines reduces ISC signature gene expression and impairs stem cell transformation

To provide information on how NSUN2 mediates *Apc*-driven hyper-proliferation, we determined the *Nsun2*-dependent transcriptome following *Apc* deletion by analysing *Apc* and *Apc Nsun2* intestinal crypts using RNA-seq. In total, we identified 1639 differentially expressed genes. Of these, 1055 genes were downregulated ($log_2FC \leq -1$, $p_{adj.} \leq 0.05$), whereas 584 genes were upregulated ($log_2FC \geq 1$, $p_{adj.} \leq 0.05$) (Fig. 5A and Table S1). Gene ontology analysis of downregulated genes found dysregulation of translation regulation, RNA processing and cell cycle regulation in *Nsun2*-loss *Vil-Apc* intestinal crypts (Fig. 5B, left). Cell apoptosis and immune activation were among the enriched upregulated processes in *Apc Nsun2*-deficient mice (Fig. 5B, right). We further the analysed this dataset using gene set enrichment analysis (GSEA). This revealed a notable enrichment in gene-sets linked with intestinal stem cell signatures and Wnt signalling targets

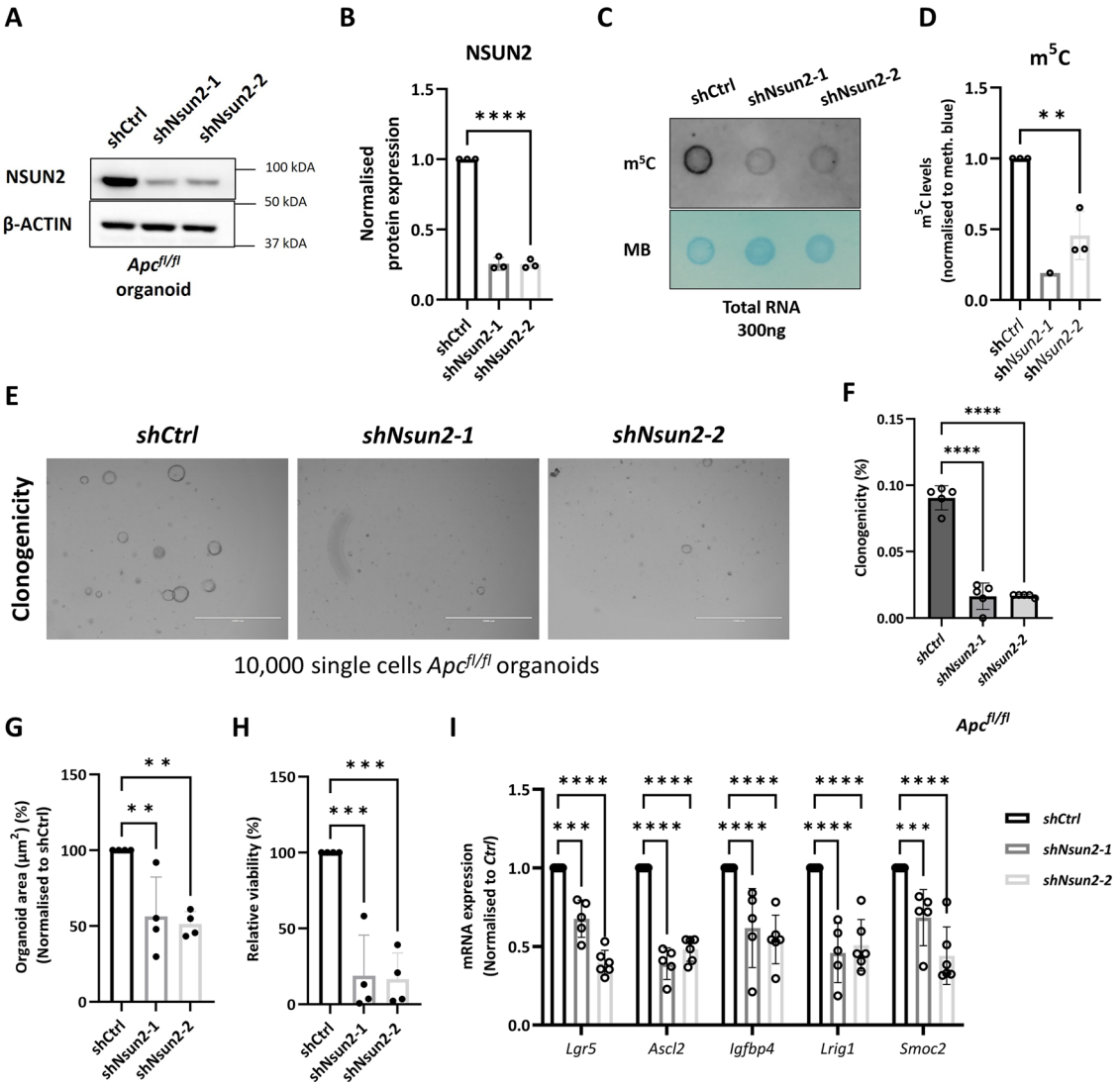

Fig. 3 NSUN2 depletion reduces stemness in *Apc*$^{fl/fl}$ mouse intestinal organoids. A Representative image of validation of Nsun2 knockdown in Vil-CreERT2 mouse *Apc*$^{fl/fl}$*-shCtrl* and *Apc*$^{fl/fl}$*-shNsun2* mouse small intestinal organoids by western blot. **B** Quantification of normalised NSUN2 protein expression levels in Vil-CreERT2 mouse *Apc*$^{fl/fl}$*-shCtrl* and *Apc*$^{fl/fl}$*-shNsun2* mouse small intestinal organoids by western blot, using β-ACTIN loading control (data are presented as mean ± SD; ****$p < 0.0001$, ordinary one-way ANOVA test compared to *shCtrl*, $n = 3$ vs. 3 biologically independent mice). **C** Representative image of 5-methylcytidine (m^5C) levels in total RNA extracted from *shNsun2-1* and *shNsun2-2* compared to *shCtrl* in *Apc*$^{fl/fl}$ mouse small intestinal organoids measured by dot blot assay. Methylene blue is used as an RNA loading control. **D** The levels of 5-methylcytidine (m^5C) in total RNA extracted from *shNsun2-1* and *shNsun2-2* compared to *shCtrl* in *Apc*$^{fl/fl}$ mouse small intestinal organoids measured by dot blot assay (data are presented as mean ± SD; **$p = 0.0092$, ordinary one-way ANOVA test compared to *shCtrl*, $n = 3$ vs. 1 vs. 3 experimental replicates). **E** Representative image of Nsun2-depletion in *Apc*$^{fl/fl}$ mouse small intestinal organoids by two best efficient *Nsun2*-targeting plasmids (*shNsun2-1 and shNsun2-2*). For *Nsun2* knockdown in *Apc*$^{fl/fl}$ organoids, transduction started on Day 1, and before puro-selection was imaged on Day 2. Puromycin selection started on Day 3, and after puro-selection was imaged on Day 6. Clonogenicity was performed on Day 9 with 10,000 single cells, and Resazurin (24 h) was measured on Day 12. **F** The percentage of raw clonogenicity levels in *shNsun2-1* and *shNsun2-2* groups compared to *shCtrl* in *Apc*$^{fl/fl}$ mouse small intestinal organoids (data are presented as mean ± SD; ****$p < 0.0001$, ordinary one-way ANOVA test compared to *shCtrl*, $n = 5$ experimental replicates). **G** The percentage of normalised organoid area (μm^2) in *shNsun2-1* and *shNsun2-2* compared to *shCtrl* in *Apc*$^{fl/fl}$ mouse small intestinal organoids (data are presented as mean ± SD; **$p = 0.0065$ (*shCtrl* vs. *shNsun2-1*), **$p = 0.0034$ (*shCtrl* vs. *shNsun2-2*), ordinary one-way ANOVA test compared to *shCtrl*, $n = 4$ experimental replicates). **H** The percentage of relative viability by Resazurin assay in *shNsun2-1* and *shNsun2-2* compared to *shCtrl* in *Apc*$^{fl/fl}$ mouse small intestinal organoids (data are presented as mean ± SD; **$p = 0.0003$ (*shCtrl* vs. *shNsun2-1*), **$p = 0.0002$ (*shCtrl* vs. *shNsun2-2*), ordinary one-way ANOVA test compared to *shCtrl*, $n = 4$ experimental replicates). **I** mRNA expression levels of stem cell markers (*Lgr5, Ascl2, Igfbp4, Lrig1, Smoc2*) verify the knockdown and show the reduction in ISC signature, respectively. All mRNA expressions were normalised to *β-actin*, a housekeeping control. All data are presented using ordinary one-way ANOVA compared to the control statistical test, $n \geq 3$ experimental replicates.

being suppressed in *Apc Nsun2* crypts, further supportive of ablated cancer stem cell function (Fig. 5C). Additional analysis demonstrated and verified this negative regulation of intestinal stem cell markers and Wnt target genes following *Nsun2* deletion (Fig. 5D). To determine the transcriptional effects of *Nsun2* deletion on normal intestine we also carried out RNAseq on *Wt* and *Nsun2* intestinal crypts. Consistent with the lack of phenotypic impact of *Nsun2* deletion on normal intestine we found far fewer transcriptional changes than in *Apc*-deficient tissue with only 4 genes downregulated and 7 genes upregulated ($log_2FC \geq 1$,

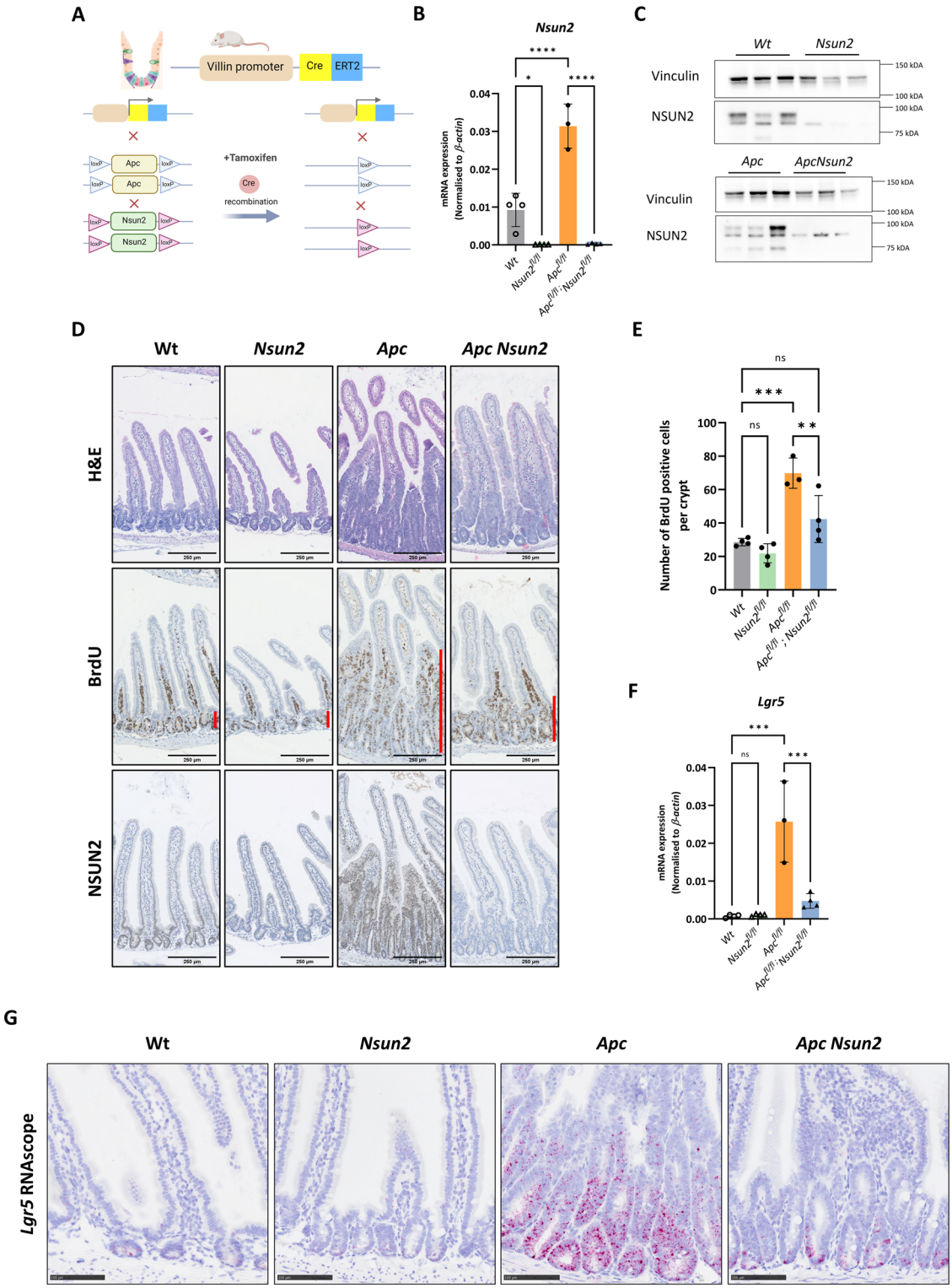

$p_{adj.} \leq 0.05$) (Table S2). Furthermore, we found no changes in expression of ISC markers or Wnt signalling targets, consistent with *Nsun2* being dispensable for normal intestinal homoeostasis (Supplementary Fig. S5A).

Due to the robust reduction in the ISC signature observed in *Nsun2*-deficient in vitro and in vivo $Apc^{fl/fl}$ tumour models, we next aimed to test whether NSUN2 is required for malignant stem cell transformation. To assess this, we used the *Lgr5-IRES-eGFP-CreERT2* model to induce intestinal adenomatous tumour formation from intestinal stem cells [2, 4, 55] (Supplementary Fig. S5B). Cohorts of *Lgr5-IRES-eGFP-CreERT2* $Apc^{fl/fl}$ (*Lgr5 Apc*), *Lgr5-IRES-eGFP-CreERT2* $Apc^{fl/fl}$ $Nsun2^{fl/fl}$ (*Lgr5 Apc Nsun2*) were generated, and tamoxifen was administered to induce gene deletion. We found that *Apc* loss-driven ISC transformation and adenoma formation were significantly impaired by *Nsun2* deletion (Fig. 5E). Together, these findings define a key role for NSUN2 in regulating ISC transformation and intestinal tumour initiation.

Fig. 4 NSUN2 deletion reduces intestinal hyperproliferation and stem cell expansion following *Apc* deletion in the mouse small intestine. **A** Schematic demonstration of *Apc* and *Nsun2* knockout mouse model generation in the intestinal tissue-specific Vil-CreERT2 line. The figure was created by Biorender.com. **B** *Nsun2* mRNA expression and knockout validation of *Nsun2* deletion in Vil-CreERT2 wild-type, $Nsun2^{fl/fl}$, $Apc^{fl/fl}$ and $Apc^{fl/fl}$ $Nsun2^{fl/fl}$ mouse small intestines by qPCR. All mRNA expressions were normalised to *β-actin*, a housekeeping control (data are presented as mean ± SD; ***$p = 0.0002$, ****$p < 0.0001$, *$p = 0.03$; one-way ANOVA test comparing the groups with each other, $n =$ minimum 3 biologically independent mice per group). **C** Validation of NSUN2 and a housekeeping control VINCULIN protein expressions in Vil-CreERT2 wild-type, $Nsun2^{fl/fl}$, $Apc^{fl/fl}$ and $Apc^{fl/fl}$ $Nsun2^{fl/fl}$ mouse small intestinal tissues by western blot ($n = 3$ biologically independent mice per group). **D** Representative images of haematoxylin and eosin (H&E), NSUN2, proliferating cells (BrdU), and β-CATENIN staining in wild-type, $Nsun2^{fl/fl}$, $Apc^{fl/fl}$, $Apc^{fl/fl}$ $Nsun2^{fl/fl}$ Vil-CreERT2 mouse small intestines. Orange lines indicate the extension of crypt regions of the small intestine. **E** Quantification of the number of BrdU-positive cells per crypt using the QuPath programme (data are presented as mean ± SD; ***$p = 0.0004$ (*Vil-Wt* vs. *Vil-*, $Apc^{fl/fl}$), **$p = 0.009$ (*Vil-*, $Apc^{fl/fl}$ vs. *Vil-*$Apc^{fl/fl}$$Nsun2^{fl/fl}$; one-way ANOVA test, $n =$ minimum 3 biologically independent mice per group). **F** mRNA expression levels of stem cell marker *Lgr5* showing the reduction in ISC signature, respectively. All mRNA expressions were normalised to *β-actin*, a housekeeping control (data are presented as mean ± SD; ***$p = 0.0001$, ***$p = 0.0001$, and ***$p = 0.0005$; One-way ANOVA test comparing the groups with each other, $n =$ minimum 3 biologically independent mice per group). **G** Representative images of *Lgr5* RNAscope in Vil-CreERT2 wild-type, $Nsun2^{fl/fl}$, $Apc^{fl/fl}$ and $Apc^{fl/fl}$ $Nsun2^{fl/fl}$ mouse small intestines. Pink dots represent the expression of *Lgr5* mRNA.

NSUN2 mediates methylation of mRNAs involved in RNA processing, stem cell fate and oncogenic MAPK/ERK signalling

NSUN2 functions as an RNA m^5C methyltransferase. Therefore, we speculated that impaired stem cell expansion following *Nsun2* deletion may be due to alterations in m^5C methylation levels. To identify the downstream mRNA targets of NSUN2-mediated m^5C methylation in intestinal homoeostasis and tumourigenesis, we performed whole transcriptome mRNA bisulfite sequencing (mRNA Bis-seq). We analysed both in vivo mouse intestinal crypts (*Vil Wt, Vil Nsun2, Vil Apc* and *Vil Apc Nsun2*) and in vitro $Apc^{fl/fl}$ organoids (*shCtrl* and *shNsun2*) (Fig. 6A, Table S3–8). Global mRNA m^5C analysis revealed significant changes in m^5C methylation in our experimental groups (Supplementary Fig. S6A). Focusing on the *Apc*-deficient models, we identified 13,374 and 11,134 differentially methylated sites (DMSs) in *Apc* vs. *Apc Nsun2* intestinal crypts and Apc^{shCtrl} vs. $Apc^{shNsun2}$ comparisons, respectively (Supplementary Fig. S6A). Interestingly, methylation changes were bidirectional, with both increased and decreased methylation observed across DMSs (Supplementary Fig. S6A). To identify common m^5C sites in the two experimentally independent groups, we intersected the differentially methylated sites from in vivo intestinal crypts (*Apc* vs *Apc Nsun2*) and 3D organoids (*shCtrl* vs *shNsun2*). We detected 525 common m^5C sites (hereafter termed in vivo vs. in vitro) (Fig. 6B) that either consistently lost methylation (295 sites) or consistently gained methylation (230 sites) (Table S9). Mapping these methylation changes to the genomic region found that sites losing methylation were enriched in gene coding regions (223/525, 43%) whilst those gaining methylation mapped predominantly to mitochondrial gene loci (Fig. 6C and Table S9).

WebLogo3 [56] motif analysis revealed enrichment of a G**C**[A/C]GGG motif in common hypo-methylated sites (Fig. 6D). This motif has previously been linked to NSUN2-mediated methylation, suggesting a conserved recognition sequence for NSUN2 activity [31, 32, 57]. Further analysis of mRNA regions showed that methylation sites altered following *Nsun2* depletion were enriched in the coding sequence (CDS; 119/525, 23%) and 3′ untranslated region (3′UTR; 135/525, 26%) although some were also found within the 5′ untranslated region (5′ UTR; 35/525, 7%) (Supplementary Fig. S6B). Across different mRNA regions, the same G**C**[A/C]GGG enriched motif was observed in sites losing methylation, suggesting this is the consensus sequence for NSUN2 activity, regardless of DMS location on the mRNA molecule (Supplementary Fig. S6C). Taken together, these data suggest NSUN2 activity is primarily directed towards specific, G-rich regions in gene-encoding mRNAs, with other methyltransferases likely responsible for methylation of mitochondrial transcripts.

To further understand the functional impact of NSUN2-dependent m^5C mRNA methylation, we investigated the function of hypomethylated mRNAs. This revealed targets of NSUN2 methylation involved in multiple cellular processes including RNA processing, stem cell function and oncogenic MAPK/ERK signalling (Fig. 6E). Regarding RNA processing, *Nsun2* depletion led to hypomethylation of genes involved in mRNA stability (*Pabpc4*), mRNA splicing (*Srsf6, Ddx39b*) and protein translation (*Rpl23, Rpl34, Eif4g1, Eif4ebp1* and *Eif4ebp2*). We also observed hypomethylation of genes involved in stem cell regulation, including *Nelfb*, which controls embryonic stem cell fate [58] and *Rela* and *Yap1*, which are previously described mediators of Wnt-driven ISC expansion and tumour initiation [4, 59–61]. We also observed hypomethylation of numerous genes involved in oncogenic MAPK/ERK signalling, including *Igfbp4, Rela, Tab1, Spag9, Mink1, Wnk2*, and *Dab2ip*. In addition to *Apc Nsun2*-deficient models, loss of methylation in several of these transcripts was also observed in normal intestine following *Nsun2* deletion, further supporting their regulation by NSUN2 (Fig. 6F). Analysis of mRNA expression levels demonstrated that these hypo-methylated transcripts were also downregulated in *Apc Nsun2*-deficient intestinal crypts compared to *Apc*-deficient controls (Fig. 6F, Table S10). Together, this indicates NSUN2 plays a key role in regulating the methylation status of mRNAs involved in RNA processing, stem cell activity and oncogenic signalling cascades, such as MAPK/ERK. Loss of m^5C methylation in these pathways leads to reduced mRNA expression, likely contributing to the impaired stem cell function and tumour initiation observed in *Apc*-deficient tissue following *Nsun2* depletion.

NSUN2 modulation of MAPK/ERK signalling mediates its oncogenic functions

As NSUN2-mediated m^5C methylation affects multiple genes involved in the MAPK/ERK signalling pathway, we next assessed whether MAPK/ERK activity is altered in cells lacking NSUN2. First, we assessed the levels of phosphorylated-ERK1/2 (p-44,42), the active form of ERK, in $Apc^{shNsun2}$ organoids. We found significantly reduced p-ERK1/2 levels compared to Apc^{shCtrl} (Fig. 7A and B). Similarly, in vivo analysis of *Apc Nsun2* mouse intestinal crypts showed a significant reduction in p-ERK1/2 levels compared to *Apc* controls (Fig. 7C and D).

To confirm these findings, we next used an $Apc^{fl/fl}$;$P53^{fl/fl}$ (*AP*) organoid model, which allows investigation of the combined effects of *Apc* loss and *P53* inactivation (which commonly occurs during CRC progression). Similar to $Apc^{fl/fl}$ organoids, depletion of *Nsun2* using shRNA in *AP* organoids (Supplementary Fig. S7A) led to diminished clonogenicity, number and area of organoid formation in addition to viability (Fig. 7E, F and Supplementary Fig. S7B). In accordance with decreased colony formation ability, expression of the stem cell marker gene, *Lgr5*, is also reduced in $AP^{shNsun2}$ organoids (Fig. 7G). Consistent with the *Apc* models, *Nsun2* depletion in AP organoid resulted in significantly reduced ERK1/2 phosphorylation (Fig. 7H and I),

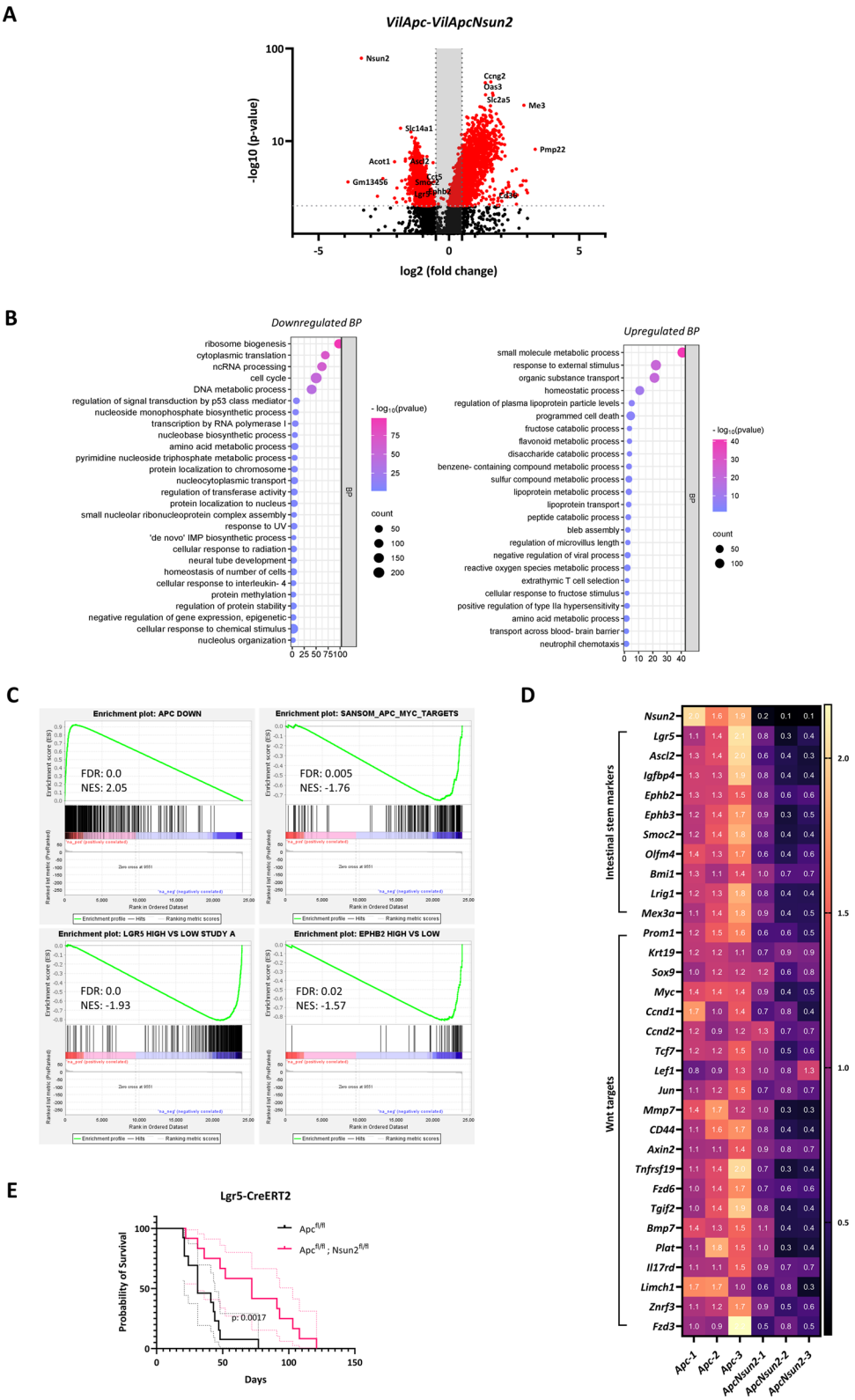

confirming that NSUN2 regulates ERK activation in *Apc*-deficient CRC models.

To functionally test the role of MAPK/ERK signalling, we tested whether constitutive activation of the pathway via $Kras^{G12D}$ mutation could bypass the requirement for NSUN2 in tumourigenesis. Using the $Apc^{fl/fl}$ $Kras^{G12D/+}$ (*AK*) organoid model, we found that the effects of *Nsun2* depletion on colony formation ability, stem cell marker expression, cell viability and p-ERK1/2 activation were reversed by $Kras^{G12D/+}$ mutation (Fig. 7J–M and Supplementary Fig. S7C, D). This suggests that the *AK* organoids, through the $Kras^{G12D/+}$ mutation, rewire the MAPK/ERK pathway, resulting in constitutive activation of MAPK/ERK signalling (Fig. 7M

Fig. 5 *Nsun2-loss* reduces stem cell signature along with Wnt-associated transcriptomic targets and improves mice survival. A The volcano plot shows the number of differentially expressed genes in *Vil-Apc* and *Vil-ApcNsun2* comparison. Differentially expressed genes (DEGs) were defined using $\log_2$FC ± 1 and $p_{adj.} \leq 0.05$. **B** Gene ontology analysis for biological process enrichment using downregulated (left) and upregulated (right) differentially expressed genes from RNA-seq comparison in *Vil-Apc* vs. *Vil-ApcNsun2* mouse small intestinal crypts. GO plots are generated using SRplot [70]. **C** Gene set enrichment analysis (GSEA)-enrichment plots of representative gene sets comparing *Vil-Apc* vs. *Vil-ApcNsun2* mouse small intestinal crypts. Negative enrichment score (NES) and FDR *q* values were shown in each panel. **D** Heat-map of differentially expressed intestinal stem cell markers and Wnt targets comparing small intestinal crypts from *Vil-Apc* vs. *Vil-ApcNsun2* mice ($n = 3$ vs. 3 biologically independent mice). **E** Probability of survival of *Lgr5-Apc* and *Lgr5-ApcNsun2* intestinal cohorts in *Lgr5-IRES-eGFP-CreERT2* mouse model. (data is presented as mean ± SD; $^{**}p = 0.0017$, as determined by Log-rank Mantel–Cox test, $n = 13$ vs. 12).

and N). To further investigate the generality of these findings, we depleted *Nsun2* in two additional *Kras* mutant models (*Apc*$^{fl/fl}$ *Kras*$^{G12D/+}$ *P53*$^{fl/fl}$*–AKP* and *Kras*$^{G12D/+}$ *P53*$^{fl/fl}$ *Notch*^{ICD}*–KPN*). In both of these models, depletion of *Nsun2* had no effect on clonogenic capacity or stem cell marker expression (Supplementary Fig. S8A–H). To test whether this effect is specific for *Apc* mutant CRC, we depleted *Nsun2* in a mutant *Braf*-driven model (*Braf*^{V600E} *P53*$^{fl/fl}$ *Notch*^{ICD}*–BPN*). The effects of *Nsun2* depletion were more modest in this model than following *Apc* deletion, suggesting it is primarily required for ISC expansion in Wnt-high CRCs (Supplementary Fig. S9A–C). Together, these findings demonstrate that NSUN2 promotes ISC expansion and CRC initiation in *Apc* mutant CRC via regulation of MAPK/ERK signalling.

DISCUSSION

In this study, we demonstrate that NSUN2 is a critical mediator of Wnt-driven intestinal stem cell transformation. Depletion of *Nsun2* impairs growth and stem cell function in *Apc*-deficient in vitro organoids and in vivo intestines while leaving healthy tissue unaffected. Furthermore, *Nsun2*-depletion suppresses tumourigenesis in a stem cell-driven model of CRC. Transcriptome-wide analysis reveals NSUN2-dependent mRNA methylation changes, particularly affecting stem cell regulators and components of the MAPK/ERK pathway. Notably, MAPK pathway activation rescues stem cell dysfunction caused by *Nsun2* loss, highlighting NSUN2's role in CRC initiation via MAPK/ERK regulation.

Previous studies have linked NSUN2 to MYC-driven proliferation and tumourigenesis in various cancers [27, 37, 45, 57, 62]. Consistent with work reported by Frye and Watt, which showed overexpression of NSUN2 in a limited number of CRC patients [37], we observed elevated NSUN2 in *Apc*-driven hyper-proliferative and malignant intestinal tissues. Increased NSUN2 expression has been reported across multiple malignancies, such as gastric [45], oesophageal [47], hepatocellular [46], bladder cancer [49] where it correlates with poor prognosis [26, 45, 47, 57]. Functional parallels also exist between our findings and previous studies. For example, Blanco et al. revealed that NSUN2-loss disrupts epidermal stem cell function and cell cycle progression, along with dysregulating site-specific tRNA methylation [36, 63]. Similarly, we observe reduced expression of intestinal CSC markers, including *Lgr5* [3], *Ephb2* [51], *Lrig1, Smoc2* and *Igfbp4*. Yet, despite a clear stem cell dysfunction following *Apc* deletion, we find no requirement for NSUN2 function in healthy intestinal stem cells. This indicates that NSUN2 is a critical mediator of Wnt-driven stem cell expansion but is dispensable for normal intestinal homoeostasis. Although our study did not investigate the effects of systemic inhibition of NSUN2 function in adult mice, it suggests NSUN2 loss is well-tolerated in the intestine. Together, these point to a potential clinical utility for NSUN2 inhibition as a suppressor of stem cell transformation and tumour initiation. Work to investigate this possibility, particularly in high-risk patient groups (those with inflammatory bowel disease, Familial adenomatous polyposis (FAP) for example) is a priority for future studies.

Using bisulfite mRNA sequencing, we identified NSUN2-dependent mRNA methylation sites in both organoids and tissues. Comparative analysis of these datasets identified 525 common regulated sites in these models. Due to the phenotypic similarity of *Nsun2* depletion in vitro and in vivo, these likely represent robust, functionally relevant m^{5}C methylation changes. Interestingly, we observed both losses and gains of m^{5}C methylation following *Nsun2* depletion. Whilst unexpected, this is similar to a recent study in the HCT15 colorectal cancer cell line showing *Nsun2*-dependent losses and gains of m^{5}C instead of a global m^{5}C reduction [64]. One possibility is the presence of other, compensating m^{5}C methyltransferases or a more complex interplay of m^{5}C regulation than previously anticipated. Analysis of *Nsun2*-dependent methylation sites led to the identification of an enrichment of G**C**[A/C]GGG dominant motif, suggesting a role for CG content in guiding NSUN2 activity. We observe this motif in all mRNA regions targeted by NSUN2, in line with the previously reported slightly different type I motif of m^{5}C, which contains a downstream G-rich triplet that has been reported in 5′UTR, CDS, and 3′UTR [30]. Similar to this, another study reported that the N1-methyladenosine (m^{1}A) modification occurs in C/G-rich sequence context [65]. The functional significance of these consensus motifs remains unclear. However, it is known that CG content significantly influences RNA structure, which may, in turn, affect translation rates. This suggests that the CG content could play a crucial role in determining how efficiently proteins are synthesised from mRNA [65]. More broadly, these motifs could help predict site-specific RNA methylation or identify novel m^{5}C regulators that specifically bind these regions.

We identified MAPK/ERK activation as a key pathway regulated by NSUN2. This is consistent with previous studies in oesophageal cancer cell lines where *NSUN2* depletion suppresses activation of PI3K/AKT and MAPK/ERK signalling, a finding that parallels our observations in organoid and in vivo CRC models. *Apc*$^{fl/fl}$ organoids with *P53* deletion are also dependent on *Nsun2* expression for maintaining stem cell function and ERK signalling. However, *Kras*$^{G12D/+}$ mutation rescues the phenotypic effects of *Nsun2* loss, suggesting *Kras*$^{G12D/+}$ sustains ERK signalling, downstream of NSUN2. Together, these findings demonstrate NSUN2 is a critical mediator of ISC expansion and tumour initiation via control of MAPK/ERK pathway activation. This defines a general mechanism by which RNA modifications mediate tumour initiation via maintenance of oncogenic signalling pathway activity.

METHODS

Ethics statement

All mouse experiments were performed under the regulations of the UK Home Office, and all related ethical regulations were adhered to. The study protocols were approved by the University of Edinburgh AWERB. All procedures were carried out within the remits of both UK Home Office Project Licence (7008885) and Personal License (I97725097).

Mouse models and experiments

All mice used in this project were housed at the Biomedical Research Facility (BRF) located at the Western General Hospital Campus of The University of Edinburgh. All mice were fed with a standard diet along with 12 h light/dark cycle. When under experiment, the mice were kept to a maximum of five per cage, but most commonly were housed in cages of

two or three. Single housing of mice is only used for the male mice separated from cage-mates due to being culled. However, single female mice were rehoused with other groups if possible. All mice were genotyped using Transnetyx (Cordoba, USA).

The alleles used in this study were as follows: Vil-CreERT2-Apc^{fl}, C57BL/6N-Nsun2$^{tm1c(EUCOMM)Wtsi/WtsiOulu}$ (Sperm) (Wellcome Trust Sanger Institute), and Lgr5-IRES-eGFP-CreERT2. To create a mixed line for co-deletion of these genes, the mice mentioned above were bred. After breeding, three different alleles (homozygote (fl/fl), heterozygote (fl/+), and wild-type (+/+)) are created for both the *Apc* and *Nsun2* genes. Subsequent matings generate cohorts of appropriate combinations of *Apc* and *Nsun2* floxed alleles for experimental use. Then, Tamoxifen induction permits conditional tissue-specific *Apc* and/or *Nsun2* ablation following Villin or Lgr5 promoter. To simplify the explanation of the studies, the mice obtained from this model will be aforementioned as follows: Vil-CreERT2-wild-type (Vil-Wt), Vil-CreERT2-Nsun2$^{fl/fl}$ (Vil-Nsun2), Vil-CreERT2-Apc$^{fl/fl}$ (Vil-Apc), and Vil-CreERT2-Apc$^{fl/fl}$;Nsun2$^{fl/fl}$ (Vil-ApcNsun2), Lgr5-IRES-eGFP-CreERT2-Apc$^{fl/fl}$ (Lgr5-Apc) Lgr5-IRES-eGFP-CreERT2-Apc$^{fl/fl}$;Nsun2$^{fl/fl}$ (Lgr5-ApcNsun2).

Tamoxifen induction

For a short-term gene deletion, Cre recombination was induced in Villin-expressing epithelium by intraperitoneal injection (IP) of Tamoxifen (Sigma-Aldrich, T5648). Mice were given a 300 µl, 10 mg/ml dose of tamoxifen on day 0 and a 200 µl, 10 mg/ml dose of tamoxifen on day 1, and a 200 µl, 10 mg/ml dose of tamoxifen on day 2. Then, mice were humanely sacrificed by cervical dislocation (CD) in line with UK Home Office regulations, and samples were collected on Day 5.

For the tumour cohort, Cre recombination was induced in Lgr5-expressing epithelium by oral gavage (OG) of tamoxifen. Mice were given a 200 µl, 10 mg/ml dose of tamoxifen for 4 consecutive days and aged. Mice were monitored, weighed, and assessed for symptoms at least twice a week. Then, mice were humanely sacrificed by CD in line with UK Home Office regulations, depending on the experiment and samples were collected. All mice were given Tamoxifen irrespective of floxed alleles, rendering wild-type mice as a control group.

in vivo labelling of cell proliferation

200 µl of Bromodeoxyuridine (BrdU), an analogue of thymidine (GE Healthcare, RPN201), was administered to mice by intraperitoneal injection for labelling of actively replicating cells 1- or 2-h prior to humanely killing.

Crypt isolation from the mouse small intestine

Once mice were humanely killed by cervical dislocation, the first 10 cm of small intestinal (SI) tissue from the mice was dissected and scraped carefully. Collected tissues were kept on ice until extraction started. SI was cut into small pieces and washed with cold PBS four times until the debris disappeared. Then, 100 µl of 0.5 M EDTA in 25 ml cold PBS was added to the small intestine pellet and placed into a roller in a cold room for 30 min. This step loosens up the crypts from the surrounding tissue. After incubation, 1:1 (v:v) Advanced DMEM/F12 (ADF) media was added on top of the EDTA-PBS solution. Then, the pellet was centrifuged at 300×*g* for 5 min and washed once with cold PBS to remove excess EDTA. After this, 2nd, 3rd and 4th fractions were collected by physical disruption using ADF media. These fractions were pooled and washed with ADF media once centrifuging at 500×*g* for 5 min, then proceeded to either crypt culture or preservation in −80 °C.

3D organoid models

Several colorectal cancer mouse organoid models (*Apc$^{fl/fl}$*, *Apc$^{fl/fl}$;Nsun2$^{fl/fl}$ AK* (*Apc$^{fl/fl}$;Kras$^{LSL\text{-}G12D/+}$*), and *AP* (*Apc$^{fl/fl}$;Tp53$^{fl/fl}$*), *Apc$^{fl/fl}$ Kras$^{G12D/+}$ P53$^{fl/fl}$* (*AKP*) and *Kras$^{G12D/+}$ P53$^{fl/fl}$ Notch^{ICD}* (*KPN*), and *Braf^{V600E} P53$^{fl/fl}$ Notch^{ICD}* (*BPN*)) were generated via crypt isolation from corresponding mouse models or obtained by the members from Dr. Kevin Myant's lab and were used. Organoids were passaged depending on genotypes, varying between 3 and 5 days, and cultured in Cultrex PathClear Reduced Growth Factor BME (Bio-Techne, 3533-010-02). The plate was incubated for 10 min at 37 °C to allow BME solidification, and 500 µl of growth medium was added. The growth medium contains Advanced DMEM/F-12 medium (ADF, Gibco) supplemented with L-Glutamine and Penicillin/Streptomycin, Primocin, 1X B27 (Gibco, 17504044), 1X N2 (Gibco, 17502048), 50 ng/ml EGF (Peprotech, 315-09-500), 100 ng/ml Noggin (Peprotech, 250-38-500). Organoids were regularly tested for Mycoplasma contamination by the facility at the Institute of Genetics and Cancer, University of Edinburgh, and found to be negative. Rest of the materials and catalogue numbers are listed in Supplementary file; Table S12.

shRNA knockdown

Plasmid constructs. Competent bacteria containing target gene set (Nsun2) plasmids (RMM3981-201810604 and RMM3981-201837916) (AAA-TAAAGGATCATCTTCAGG and AAGTCTAGGTATGCTGGATGC) were ordered from Horizon Discovery. Competent bacteria containing mouse Nsun2 shRNA plasmids, as well as bacteria containing pLKO.1 plasmids (as a control) were grown in L-ampicillin plates overnight in a 37 °C incubator. Next day, single colonies were picked and cultured in liquid L-broth culture supplemented with L-ampicillin (50 mg/ml) in 37 °C shaker overnight. Subsequently, plasmids were isolated by QIAGEN Plasmid Midi (#200119) or Maxi Kit (#12662).

Lentiviral production. 10 µg of a gene-specific lentiviral vector was mixed with 7.5 µg of the lentiviral packaging vector psPAX2 (Addgene) and 2.5 µg of the envelope protein-producing vector pCMV-VSV-G (Addgene). This mixture was then transfected into HEK 293T cells cultured in a 10 cm² dish using the polyethylenimine transfection reagent (Polysciences, 23966). After 48 h, the virus was purified by filtering the supernatant media with a 0.45 µm filter, followed by concentration using the Lenti-X Concentrator (Takara Bio, 631232) and resuspension of the viral particles in PBS.

Lentiviral transduction of mouse colorectal cancer organoid models. Firstly, organoids were pre-treated with 1:10,000 valproic acid (VPA) on Day (−1). On Day 1, organoids were dissociated into single cells with 1 ml pre-warmed StemPro Accutase for 2 min at 37 °C. The dissociation was stopped using 1 ml of filtered 1% BSA in PBS. Resuspension was filtered and centrifuged at 300×*g* for 3 min at 4 °C. The pellet was resuspended in transduction media containing culture media and 8 µg/ml Polybrene, 2 µl Y27632 Rock Inhibitor (1:500), and Valproic acid (VPA) (1:10,000). The number of single cells was counted using an automatic cell count (Countess II System). 100,000 cells containing 10 µl virus per well were seeded into a pre-coated plate with BME and incubated at 37 °C for 24 h. Media containing organoid-virus-polybrene sets on the BME monolayer. On Day 2, media containing the virus was removed, 100 µl BME was added per well. Once BME was set, organoids were grown in culture media with 2 µl Y27632 Rock Inhibitor (1:500). On Day 3, media was replaced with 2 µg/ml Puromycin and incubated at 37 °C for 72 h. Puromycin selection kills non-transduced organoids. On Day 6, RNA and protein samples were isolated and reserved at −80 °C, or a clonogenicity assay was performed. The organoids were incubated at 37 °C, 0.5% CO_2 throughout the experiments.

Analysis of colony formation ability and metabolic activity by clonogenicity and Resazurin assay

The organoids were dissociated into single cells 6 days after the lentiviral transduction. 10,000 single cells (*Apc$^{fl/fl}$*) and 2000 single cells (*AK* and *AP*), 1000 single cells (*AKP, KPN, BPN*) in 5 µl BME were seeded to a 12-well plate. Sphere formation was observed following 2–4 days. Then, spheres were counted on a Leica Light microscope, and pictures were taken on the EVOS FL Cell Imaging System.

Once the organoid spheres were formed, the clonogenicity was counted, and the media were replaced with fresh media containing 10% Resazurin for 24 h in a 37 °C incubator. The next day, relative cell viability was measured by a multi-label counter Victor 21420 or TECAN Spark microplate reader in a 96-well plate with three technical replicates.

Total RNA and mRNA purification

RNA samples from mouse intestinal tissues, cell lines and organoid cultures were isolated by using the RNeasy® Mini Kit following the manufacturer's protocol. Subsequently, the DNA degradation step was used as an additional step using the RNase-Free DNase Set. RNA samples were analysed for quality and quantity using Thermo Scientific™ Nanodrop™ (Thermo Fisher).

To purify poly(A) mRNA, total RNA was subjected to oligo (dT)25 magnetic beads to capture poly(A) containing mRNA. The manufacturer's protocol was used with several adjustments. Firstly, 30–40 µg total RNA was incubated at 70 °C for 5 min to disrupt secondary structures and placed on ice. Then, lysis/binding buffer suspensions were prepared according to the manufacturer's instructions. During the binding step, RNA samples added to Dynabeads/binding buffer were mixed for 20 min at

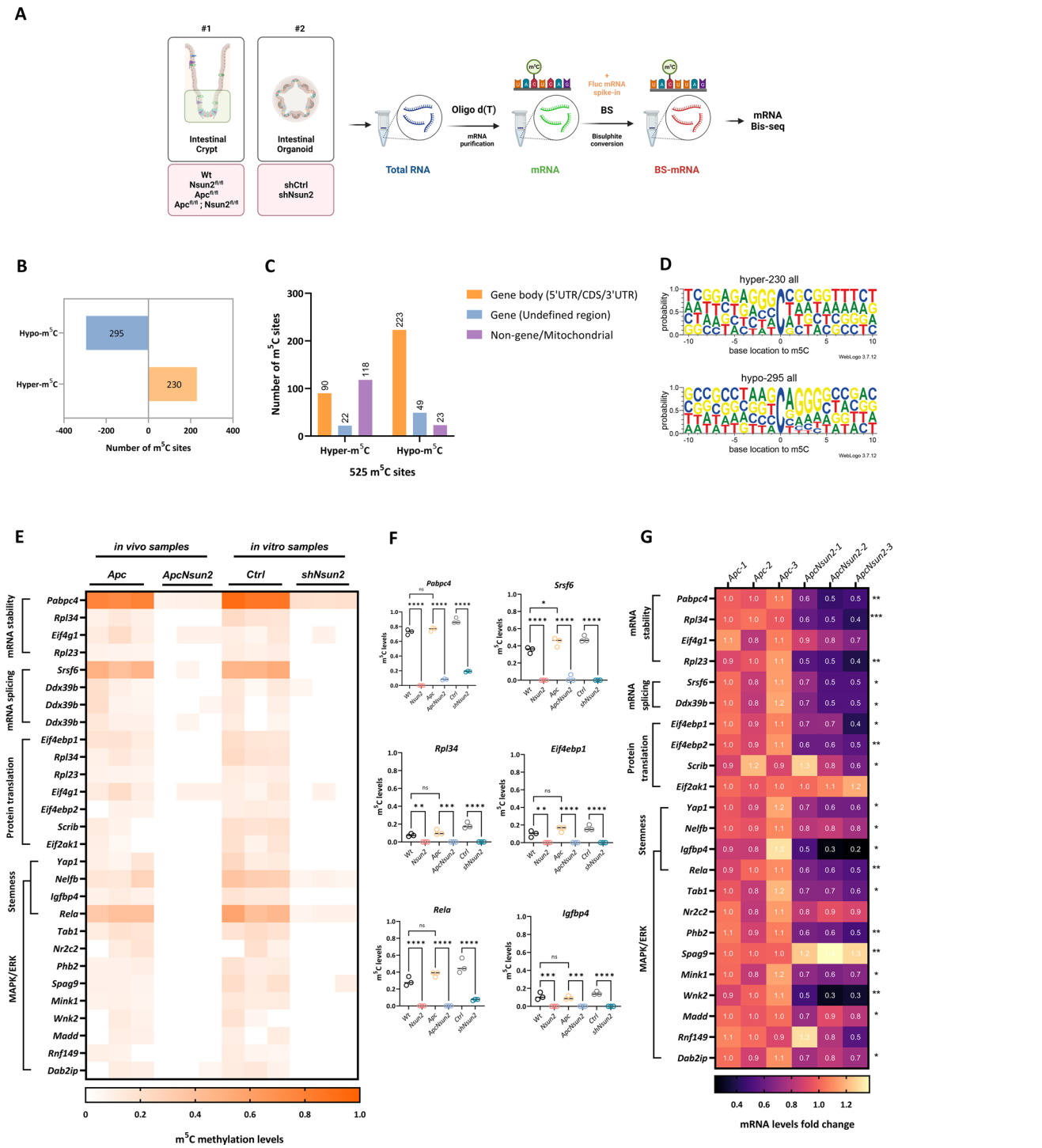

Fig. 6 ***Nsun2*-loss leads to bi-directional transcriptomic m^{5}C signature in *Apc-deficient* intestines. A** Schematic demonstration of workflow and experimental models used in whole transcriptome bisulfite sequencing. The figure was created using Biorender.com. **B** The bar graph shows the number of m^{5}C sites that are common methylation gain and loss between *Vil-Apc* vs. *Vil-ApcNsun2* and *shCtrl* vs. *shNsun2* comparison. Differentially methylated sites (DMSs) were defined using Δmethylation ratio: ±0.05. **C** Bar graph showing the number of hyper- and hypomethylated sites identified in different genomic regions. **D** The probability pattern represents the sequence context of 10 bases up and downstream of hypo-methylated and hyper-methylated common 525 NSUN2-dependent m^{5}C sites as a result of overlapping vivo and vitro m^{5}C sites. **E** Heat-map of differentially methylated sites in mRNA stability, mRNA splicing, protein translation, stemness, and MAPK/ERK cascade in *Vil-Wt* vs. *Vil-Nsun2, Vil-Apc* vs. *Vil-ApcNsun2* intestinal crypts, and *shCtrl* vs. *shNsun2* organoids ($n = 3$ vs. 3 biologically independent mice or experimental replicates). **F** mRNA m^{5}C methylation levels in some of the selected mRNAs involved in mRNA stability (*Pabpc4, Rpl34*), mRNA splicing (*Srsf6*), protein translation (*Eif4ebp1*), stemness and MAPK/ERK cascade (*Rela* and *Igfbp4*) in *Vil-Wt* vs. *Vil-Nsun2, Vil-Apc* vs. *Vil-ApcNsun2* intestinal crypts and *shCtrl* vs. *shNsun2* by mRNA-bis-seq (data are presented as mean; ***$p < 0.001$, **$p < 0.01$, *$p < 0.05$; One-way ANOVA test comparing the groups each other, $n = 3$ vs. 3 biologically independent mice or experimental replicates). **G** Heat-map of mRNA levels in mRNA stability, mRNA splicing, protein translation, stemness, and MAPK/ERK cascade in *Vil-Apc* vs. *Vil-ApcNsun2* intestinal crypts by RNA-seq (***$p < 0.001$, **$p < 0.01$, *$p < 0.05$; unpaired *t*-test, $n = 3$ biologically independent mice per group).

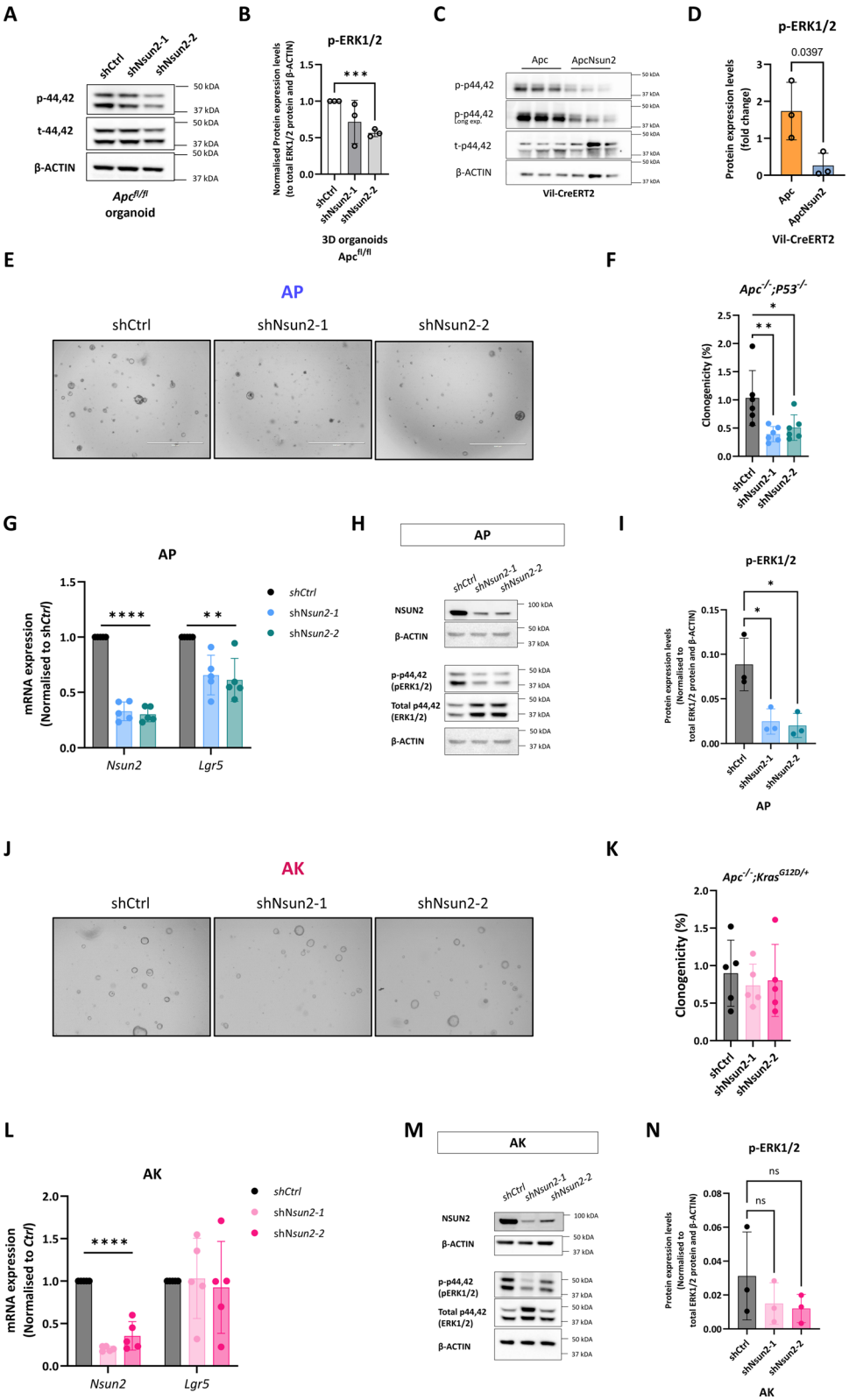

room temperature with gentle rotation at 5–10 rpm for annealing of the mRNA to oligo (dT)25 magnetic beads. The mRNA-beads complex was washed twice before and eluted with 10 mM Tris–HCl at 70 °C for 5 min. Finally, the enriched mRNA concentration was determined by Nanodrop, and the purity was analysed by Bioanalyzer Agilent RNA 6000 Nano/Pico assay (Agilent, Santa Clara, CA).

cDNA synthesis and RT-qPCR

cDNA was generated by reverse transcription of the isolated RNA using qScript™ cDNA SuperMix with three RT-PCR cycles; 25 °C for 5 min, 42 °C for 30 min, 72 °C for 15 min, 4 °C forever. qPCR performed according to the manufacturer's protocol using fast SYBR Select Master Mix. Primer sequences are listed in Supplementary file; Table S13. Amplifications were

Fig. 7 NSUN2 mediates MAPK activation. A Representative image of validation of Nsun2 mediating MAPK/ERK signalling through phospho-ERK1/2 (p-44,42) in *Apc$^{fl/fl}$-shCtrl* and *Apc$^{fl/fl}$-shNsun2* mouse small intestinal organoids by western blot. **B** Quantification of normalised phospho-ERK1/2 (p-44,42) protein expression levels in *Apc$^{fl/fl}$-shCtrl* and *Apc$^{fl/fl}$-shNsun2* mouse small intestinal organoids by western blot, using β-ACTIN-loading control (data are presented as mean ± SD; ***$p = 0.0001$, two-tailed *t*-test, $n = 3$ experimental replicates). **C** Representative image of validation of Nsun2 mediating MAPK/ERK signalling through phospho-ERK1/2 (p-44,42) in *Vil-Apc* vs. *Vil-ApcNsun2* intestinal crypts by western blot. **D** Quantification of normalised phospho-ERK1/2 (p-44,42) protein expression levels in *Vil-Apc* vs. *Vil-ApcNsun2* intestinal crypts by western blot, using β-ACTIN loading control (data are presented as mean ± SD; *$p = 0.0397$, two-tailed *t*-test, $n = 3$ vs. 3 biologically independent mice). **E** Representative image of Nsun2-depletion in *Apc$^{fl/fl}$; P53$^{fl/fl}$ (AP)* mouse small intestinal organoids by two best efficient *Nsun2*-targeting plasmids (*shNsun2-1 and shNsun2-2*). For *Nsun2* knockdown in *AP* organoids, transduction started on Day 1, and before puro-selection was imaged on Day 2. Puromycin selection started on Day 3, and after puro-selection was imaged on Day 6. Clonogenicity was performed on Day 9 with 2000 single cells, and Resazurin (24 h) was measured on Day 12. **F** The percentage of raw clonogenicity levels in *shNsun2-1* and *shNsun2-2* groups compared to *shCtrl* in *Apc$^{fl/fl}$; P53$^{fl/fl}$ (AP)* mouse small intestinal organoids (data are presented as mean ± SD; **$p = 0.0065$ and *$p = 0.023$, ordinary one-way ANOVA test compared to *shCtrl*, $n = 6$ experimental replicates). **G** Validation of *Nsun2* knockdown and mRNA expression level of stem cell marker gene *Lgr5* in *Apc$^{fl/fl}$* mouse small intestinal organoids by qPCR. All mRNA expressions were normalised to *β-actin*, a housekeeping control (data are presented as mean ± SD; ****$p < 0.0001$, **$p = 0.0073$ and **$p = 0.0032$, ordinary one-way ANOVA test compared to *shCtrl*, $n = 5$ experimental replicates). **H** Representative image of validation of NSUN2 depletion and NSUN2 mediating MAPK/ERK signalling through phospho-ERK1/2 (p-44,42) in *Apc$^{fl/fl}$; P53$^{fl/fl}$ (AP)* mouse small intestinal organoids following Nsun2-knockdown intestinal crypts by western blot. β-ACTIN used as loading control. **I** Quantification of normalised phospho-ERK1/2 (p-44,42) protein expression levels in *Apc$^{fl/fl}$; P53$^{fl/fl}$ (AP)-shCtrl* and *Apc$^{fl/fl}$; P53$^{fl/fl}$ (AP)-shNsun2* mouse small intestinal organoids by western blot, using β-ACTIN-loading control (data are presented as mean ± SD; *$p = 0.0152$ and *$p = 0.0113$, ordinary one-way ANOVA test compared to *shCtrl*, $n = 3$ experimental replicates). **J** Representative image of Nsun2-depletion in *Apc$^{fl/fl}$; Kras$^{G12D/+}$ (AK)* mouse small intestinal organoids by two best efficient *Nsun2*-targeting plasmids (*shNsun2-1* and *shNsun2-2*). For *Nsun2* knockdown in *AP* organoids, transduction started on Day 1, and before puro-selection was imaged on Day 2. Puromycin selection started on Day 3, and after puro-selection was imaged on Day 6. Clonogenicity was performed on Day 9 with 2000 single cells, and Resazurin (24 h) was measured on Day 12. **K** The percentage of raw clonogenicity levels in *shNsun2-1* and *shNsun2-2* groups compared to *shCtrl* in *Apc$^{fl/fl}$; Kras$^{G12D/+}$ (AK)* mouse small intestinal organoids (data are presented as mean ± SD; not significant values are not indicated, ordinary one-way ANOVA test compared to *shCtrl*, $n = 5$ experimental replicates). **L** Validation of *Nsun2* knockdown and mRNA expression level of stem cell marker gene *Lgr5* in *Apc$^{fl/fl}$; Kras$^{G12D/+}$ (AK)* mouse small intestinal organoids by qPCR. All mRNA expressions were normalised to *β-actin*, a housekeeping control (data are presented as mean ± SD; ****$p < 0.0001$, not significant values are not indicated, ordinary one-way ANOVA test compared to *shCtrl*, $n = 5$ experimental replicates). **M** Representative image of validation of NSUN2 depletion and NSUN2 mediating MAPK/ERK signalling through phospho-ERK1/2 (p-44,42) in *Apc$^{fl/fl}$; Kras$^{G12D/+}$ (AK)* mouse small intestinal organoids following Nsun2-knockdown intestinal crypts by western blot. β-ACTIN used as loading control. **N** Quantification of normalised phospho-ERK1/2 (p-44,42) protein expression levels in *Apc$^{fl/fl}$; Kras$^{G12D/+}$ (AK)-shCtrl* and *Apc$^{fl/fl}$; Kras$^{G12D/+}$ (AK)-shNsun2* mouse small intestinal organoids by western blot, using β-ACTIN-loading control (data are presented as mean ± SD; ordinary one-way ANOVA test compared to *shCtrl*, $n = 3$ experimental replicates).

performed in two experimental replicates in a 384-well plate using CFx Touch 384 (BioRad). β-Actin or Gapdh primers were used as a housekeeping control. Ct-values were normalised to β-Actin or Gapdh Ct-values. mRNA expression levels were calculated according to the ΔCt method and expressed as $2(-\Delta Ct)$.

Protein isolation and quantification

Samples were washed with 1X cold PBS and centrifuged at 2000 rpm for 5 min. The pellet was resuspended with RIPA buffer (Sigma, #R0278) containing 10% (v/v) Proteinase and Phosphatase inhibitor cocktails and incubated on ice for 30–45 min. Then, proteins were isolated after centrifuging at 14,000 rpm at 4 °C for 10 min and the isolated proteins were stored at −80 °C. Isolated proteins were quantified using the PierceTM BCA assay kit (Thermo Fisher).

Western blot

Protein samples were prepared using 4X loading buffer (DTT) and denatured at 99 °C for 5 min. After being immediately taken on ice, 15 µg of proteins were loaded and run in a 4–12% Bis–Tris or 3–8% Tris–Acetate gel at 150 V for 1 h. Then proteins were transferred to a nitrocellulose membrane by wet-western blotting technique. After transfer, membranes were stained with Ponceau S dye. Subsequently, the membranes were blocked, incubated with primary and corresponding HRP-linked secondary antibodies for each antibody, as shown in Supplementary file; Table S11. Finally, image visualisation was performed using chemiluminescent ECL substrates in Amersham ImageQuant 800. The quantification of the blots was performed using ImageJ68.

For stripping. The membranes were washed in 1X ReBlot Plus Strong Antibody Stripping Solution Reblot (Merck, #2504) for 10 min and washed with PBST for 10 min prior to re-blocking and re-incubation with new antibody. The membranes were stripped a maximum of two times. Rest of the materials and catalogue numbers are listed in Supplementary file; Table S12. Uncropped western blot images are shown in the Supplementary file, Western blots.

Dot blot

RNA samples were serially diluted (100–300 ng in total volume 4–7 µl) and denaturised at 95 °C for 5 min to disrupt secondary structures on Day 1. Then, RNA samples were immediately chilled on ice for 1 min to prevent re-formation of secondary structures, and samples were dropped onto Hybond-N+ membrane. The membrane was air-dry for 5 min and RNA samples were crosslinked to the membrane by Stratalinker 2400 UV Crosslinker twice using the Autocrosslink mode (1200 microjoules [×100]; 25–50 s). The membrane was directly blocked with LICOR blocking buffer, incubated with primary and corresponding HRP-linked secondary antibodies for each antibody, as shown in the Supplementary file. Finally, image visualisation was performed using chemiluminescent ECL substrates in Amersham ImageQuant 800. The quantification of the blots was performed using ImageJ.

Tissue sampling

Following BrdU labelling and humane killing, small intestine and colon tissues were dissected from the mice. The gut was initially flushed with PBS to clean the lumen, opened longitudinally, pinned to a flat surface, and fixed with paraformaldehyde for 20 min at room temperature in the case of a Swiss-roll of the gut. Otherwise, three pieces of gut were cut and put together in a PFA-containing tube, called a parcel. Then, fixations continued overnight at 4 °C. After 24 h, samples were transferred into 70% Ethanol. After fixation of the tissues, the Tissue Tek® (Sakura) VIP processor was used to process the samples before being embedded in paraffin wax. After being embedded, 5 µm sections of tissues were cut and dried overnight at 37 °C incubator for further analysis, H&E or immunohistochemistry.

For haematoxylin and eosin (H&E) staining. Tissue sections on slides were dewaxed in three cycles of Xylene for 5 min in each, two cycles of 100% Ethanol, then one cycle of 75%, 50%, and 25% Ethanol for 2 min in each, consecutively. Slides were then washed and incubated in haematoxylin for 90 s. After this, slides were washed with water for 2 min, and left in lithium carbonate for 5 s to develop the signal, and washed quickly. Then, the slides were incubated in Eosin dye for 40 s to counterstain and washed again. Subsequently, slides were dehydrated in the opposite direction of

the dewaxing solutions and finally were mounted using DPX.

For standard IHC techniques and details, see Supplementary file; Table S11. To scan the slides, Nanozoomer (Hammamatsu), and to image the slides, NDP-image and QuPath software were used.

Lgr5 RNAscope

Detection of Lgr5 mRNA was performed using the RNAscope™ 2.5 HD Assay—RED kit (#322360, ACDBio) according to the manufacturer's instructions. The slides underwent target retrieval at 98–102 °C for 15 min on a hot plate, followed by a wash in 100% Ethanol for 1 min. Protease Plus treatment was carried out for 30 min at 40 °C. Hybridisation was performed using the RNAscope™ Probe—Mm-Lgr5 (Cat. No. 312171) for 2 h at 40 °C. For each tissue sample, both negative and positive controls were included to verify tissue integrity and assay performance.

RNA sequencing

For RNA sequencing, the quality of total RNA samples was initially assessed on the Agilent 2100 Electrophoresis Bioanalyser Instrument (Agilent Technologies Inc, #G2939AA) and RNA 6000 Nano chips (#5067-1511) at IGC Technical Service. Then, the total RNA samples were sent to the Wellcome Trust Clinical Research Facility (WTCRF) at the Western General Hospital, Edinburgh. All subsequent analyses for RNA sequencing were handled at WTCRF. The total RNAs were re-assessed using Qubit 2.0 Fluorimeter (Thermo Fisher Scientific Inc, #Q32866), Qubit RNA broad range assay kit (# Q10210), and the Qubit dsDNA HS assay kit (#Q32854) prior to library preparation. Then, libraries were prepared from 500 ng of each total RNA sample using the NEBNEXT Ultra II Directional RNA Library Prep kit (NEB #7760) and the Poly(A) mRNA magnetic isolation module (NEB #E7490) according to the provided protocol. Subsequently, sequencing was performed on the NextSeq 2000 platform (Illumina Inc, #20038897) using NextSeq 2000 P2 Reagents (200 Cycles) (##20046812). Each library ended up with more than 24 million paired-end reads. Raw FASTQ files were then uploaded for RNAseq analysis. To analyse differentially expressed genes, an interactive RaNA-seq tool was used. For functional analysis, g:Profiler, and gene set enrichment analysis (GSEA) platforms were used.

mRNA bisulfite treatment

mRNA Bisulfite treatment was performed according to the manufacturer's protocol in the EZ RNA Methylation™ Kit. One cycle of mRNA conversion steps by PCR is as follows: 70 °C 10 min, 64 °C 45 min, and 4 °C.

mRNA bisulfite sequencing

The bisulfite-treated mRNA samples were assessed on an Agilent 2100 Electrophoresis Bioanalyser Instrument using RNA 6000 Pico chips at IGC Technical Service. Then, the samples were sent to WTCRF and were re-assessed by Qubit 2.0 Fluorimeter (Thermo Fisher Scientific Inc., #Q32855) and the Qubit RNA high sensitivity assay kit (# Q10210) prior to library preparation. After the quality control steps, the libraries were prepared from 10 ng of each bisulfite-treated mRNA sample using protocol 4 (library preparation for poly(A)-purified mRNA or rRNA-depleted RNA) NEBNEXT Ultra II Directional RNA Library Prep kit (NEB #7760). The mRNAs were fragmented. Subsequently, sequencing was performed on the NextSeq 2000 platform (Illumina Inc., #20038897) using NextSeq 2000 P3 Reagents (200 Cycles) (#20040560). Each library ended up with more than 46 million paired-end reads. Raw FASTQ files were then uploaded for the m^{5}C-mRNA analysis.

mRNA-Bis-seq analysis for 5-methylcytidine

Low-quality reads ($Q < 20$) and adaptor contaminations were removed by FASTQC and Trim Galore! tools on Galaxy (https://usegalaxy.org/). The argument in the Trim Galore tool is to remove non-original sequence in the samples; read 1 '-j 1 -e 0.1 -q 20 -O 1-a AGATCGGAAGAGCACACGTCTGAACTCCAGTCAC' and read 2 '-j 1 -e 0.1 -q 20 -O 1-a AGATCGGAAGAGCGTCGTGTAGGGAAAGAGTGTAGATCTCGGTGGTCGCCGTATCATT'.

Then, trimmed and high-quality reads were aligned to an in silico bs-converted mouse reference genome (GRCm39, Release-107 in (http://www.ensembl.org/Mus_musculus/Info/Index website) by gene transfer format (GTF) using meRanGh align within meRanTK tool54 kits (Version 1.2.1b). This step also included a splice-aware HISAT2 algorithm and arguments '-mmr 0.1'. Subsequently, SAM files were obtained and proceeded to conduct the identification of m5C sites using the arguments as follows: '-rl 150 -md 5 -ei 0.1 -cr 99 -fdr 0.01 -mcov 10 -mr 0.05'. The criteria used to filter m^{5}C sites are: minimum 10 reads coverage, methylation ratio over 5% (0.05), and false discovery rate 1%. Then, gene annotation for m^{5}C sites was retrieved by using meRanAnnotate with the general feature format 3 (GFF3).

mRNA bisulfite sequencing (remarks)

We used almost 40 µg of total RNA for poly(A) purification and ~38–138 ng/µl of bs-treated mRNA for next-generation sequencing. Most of the purified mRNAs in our experimental groups range between 1% and 4% of the corresponding total RNAs, which is in line with previous mRNA-Bis-seq studies [57]. Prior to poly(A) purification and NGS, total RNA and mRNA integrity were assessed by Bioanalyzer to prove undegraded samples. Afterwards, poly(A) purified mRNAs were pooled with luciferase spike-in control (1:10,000 ratio) derived from another species (*Photinus pyralis*, a.k.a. Firefly) and does not contain any m^{5}C sites before bisulfite conversion. The average reads in our samples are 66.7M per sample. After trimming and quality control, the high-quality reads are mapped into an in silico bs-converted mouse reference genome (GRCm39) and luciferase spike-in control using meRanTK tools [66]. We found that both our samples and spike-in controls were almost ~99.8% converted (Supplementary Table S4), which ensures the efficiency of bisulfite conversion of non-methylated cytosines in the samples. This finding is convincingly similar to previous studies [57, 67].

Various studies on different tissue and cell types have reported a range of cut-off values [28, 30, 31, 57, 68] using the meRanTK tool [66]. This implies cell-context dependency in mRNA m^{5}C methylation. Therefore, it is crucial to identify candidate m^{5}C mRNA selection criteria in our samples. After a round of optimisation, we selected the following criteria in meRanCall: minimum reads coverage (mcov): 10, methylation ratio (mr) ≥ 0.05, and false discovery rate (FDR) = 1%. Using this selection, we detected nearly 100,000 m^{5}C sites for each in vivo sample and 50,000–100,000 m^{5}C sites in the in vitro samples. Looking into luciferase spike-in control, we generally determined 1–2 m^{5}C sites per sample, except for the wild-type-3 sample (Supplementary Table S3). Following these, we realised that some sites are missing from the analysis. This is because of obscured sites where m^{5}C is completely lost in the *Nsun2*-loss samples. To revise this, we also included "mr:0 only" values. In this way, we did not discard the mr:0 sites, but this might cause a background noise. To overcome this challenge, we also set the standard deviation between replicates within each group to be lower than 0.1.

Meta-analysis of TCGA data

Human colorectal cancer datasets (TCGA-COAD and TCGA-READ PanCancer) were retrieved from cBioPortal. The expressions of gene of interests within the TCGA-COAD and TCGA-READ patient datasets were analysed by using the cBioPortal and XenaBrowser platforms. Several CRC classifications were also obtained from Xenabrowser and the Myant lab. For the survival analysis, Cox regression hazard model and Kaplan–Meier analysis were conducted using PanCancer datasets in KM-PLOT. Figures plotted in GraphPad Prism 9.5.1.

Statistical analysis

Unpaired *t*-test and one-way ANOVA multiple comparison tests were used by GraphPad Prism Software version 9.5.1 for Windows (GraphPad Software, San Diego, CA). Statistically significant changes were shown by a symbol (*). Symbol expressions are as follows: $*P < 0.05$ (significant); $**P < 0.01$ (very significant); $***P < 0.001$ and $****P < 0.0001$ (extremely significant), and ns: non-significant.

DATA AVAILABILITY

RNAseq and mRNA bisulfite-sequencing generated in this study have been uploaded into the Genome Sequence Archive (https://ngdc.cncb.ac.cn/gsa/) website with the following accession numbers: CRA037492 (RNAseq) and CRA037494 (mRNABisseq). All data reported in this paper and any additional information will be shared upon reasonable request to the lead contact.

CODE AVAILABILITY

RNAseq and mRNA bisulfite sequencing generated in this study have been uploaded into the Genome Sequence Archive (https://ngdc.cncb.ac.cn/gsa/) website with the following accession numbers: CRA037492 (RNAseq) and CRA037494 (mRNABisseq).

All data reported in this paper and any additional information will be shared upon reasonable request to the lead contact.

REFERENCES

1. Ferlay J, Ervik M, Lam F, Laversanne M, Colombet M, Mery L, Piñeros M, Znaor A, Soerjomataram I, Bray F (2024). Global Cancer Observatory: Cancer Today (version 1.1). Lyon, France: International Agency for Research on Cancer. Available from: https://gco.iarc.who.int/today, accessed [16 March 2026].
2. Barker N, Ridgway RA, van Es JH, van de Wetering M, Begthel H, van den Born M, et al. Crypt stem cells as the cells-of-origin of intestinal cancer. Nature. 2009;457:608–11.
3. Barker N, van Es JH, Kuipers J, Kujala P, van den Born M, Cozijnsen M, et al. Identification of stem cells in small intestine and colon by marker gene Lgr5. Nature. 2007;449:1003–7.
4. Myant KB, Cammareri P, McGhee EJ, Ridgway RA, Huels DJ, Cordero JB, et al. ROS production and NF-κB activation triggered by RAC1 facilitate WNT-driven intestinal stem cell proliferation and colorectal cancer initiation. Cell Stem Cell. 2013;12:761–73.
5. Drost J, van Jaarsveld RH, Ponsioen B, Zimberlin C, van Boxtel R, Buijs A, et al. Sequential cancer mutations in cultured human intestinal stem cells. Nature. 2015;521:43–7.
6. Fearon ER, Vogelstein B. A genetic model for colorectal tumorigenesis. Cell. 1990;61:759–67.
7. Matano M, Date S, Shimokawa M, Takano A, Fujii M, Ohta Y, et al. Modeling colorectal cancer using CRISPR-Cas9-mediated engineering of human intestinal organoids. Nat Med. 2015;21:256–62.
8. Korinek V, Barker N, Morin PJ, van Wichen D, de Weger R, Kinzler KW, et al. Constitutive transcriptional activation by a beta-catenin-Tcf complex in APC−/− colon carcinoma. Science. 1997;275:1784–7.
9. Rubinfeld B, Albert I, Porfiri E, Fiol C, Munemitsu S, Polakis P. Binding of GSK3beta to the APC–beta-catenin complex and regulation of complex assembly. Science. 1996;272:1023–6.
10. Ooki A, Shinozaki E, Yamaguchi K. Immunotherapy in colorectal cancer: current and future strategies. J Anus Rectum Colon. 2021;5:11–24.
11. Van Cutsem E, Köhne CH, Hitre E, Zaluski J, Chang Chien CR, Makhson A, et al. Cetuximab and chemotherapy as initial treatment for metastatic colorectal cancer. N Engl J Med. 2009;360:1408–17.
12. Xie YH, Chen YX, Fang JY. Comprehensive review of targeted therapy for colorectal cancer. Signal Transduct Target Ther. 2020;5:22.
13. de Sousa e Melo F, Kurtova AV, Harnoss JM, Kljavin N, Hoeck JD, Hung J, et al. A distinct role for Lgr5(+) stem cells in primary and metastatic colon cancer. Nature. 2017;543:676–80.
14. Ramadan R, van Driel MS, Vermeulen L, van Neerven SM. Intestinal stem cell dynamics in homeostasis and cancer. Trends Cancer. 2022;8:416–25.
15. Rehman SK, Haynes J, Collignon E, Brown KR, Wang Y, Nixon AML, et al. Colorectal cancer cells enter a diapause-like DTP state to survive chemotherapy. Cell. 2021;184:226–42.e21.
16. Vermeulen L, de Sousa e Melo F, Richel DJ, Medema JP. The developing cancer stem-cell model: clinical challenges and opportunities. Lancet Oncol. 2012;13:e83–9.
17. Motorin Y, Helm M. tRNA stabilization by modified nucleotides. Biochemistry. 2010;49:4934–44.
18. Squires JE, Patel HR, Nousch M, Sibbritt T, Humphreys DT, Parker BJ, et al. Widespread occurrence of 5-methylcytosine in human coding and non-coding RNA. Nucleic Acids Res. 2012;40:5023–33.
19. Chow CS, Lamichhane TN, Mahto SK. Expanding the nucleotide repertoire of the ribosome with post-transcriptional modifications. ACS Chem Biol. 2007;2:610–9.
20. Dai X, Gonzalez G, Li L, Li J, You C, Miao W, et al. YTHDF2 binds to 5-methylcytosine in RNA and modulates the maturation of ribosomal RNA. Anal Chem. 2020;92:1346–54.
21. Boriack-Sjodin PA, Ribich S, Copeland RA. RNA-modifying proteins as anticancer drug targets. Nat Rev Drug Discov. 2018;17:435–53.
22. Pan J, Huang Z, Xu Y. m5C RNA methylation regulators predict prognosis and regulate the immune microenvironment in lung squamous cell carcinoma. Front Oncol. 2021;11:657466.
23. Boccaletto P, Stefaniak F, Ray A, Cappannini A, Mukherjee S, Purta E, et al. MODOMICS: a database of RNA modification pathways. 2021 update. Nucleic Acids Res. 2022;50:D231–d5.
24. Amos H, Korn M. 5-Methyl cytosine in the RNA of Escherichia coli. Biochim Biophys Acta. 1958;29:444–5.
25. Tuorto F, Liebers R, Musch T, Schaefer M, Hofmann S, Kellner S, et al. RNA cytosine methylation by Dnmt2 and NSun2 promotes tRNA stability and protein synthesis. Nat Struct Mol Biol. 2012;19:900–5.
26. Yang M, Wei R, Zhang S, Hu S, Liang X, Yang Z, et al. NSUN2 promotes osteosarcoma progression by enhancing the stability of FABP5 mRNA via m(5)C methylation. Cell Death Dis. 2023;14:125.
27. Zhang G, Liu L, Li J, Chen Y, Wang Y, Zhang Y, et al. NSUN2 stimulates tumor progression via enhancing TIAM2 mRNA stability in pancreatic cancer. Cell Death Discov. 2023;9:219.
28. Yang X, Yang Y, Sun B-F, Chen Y-S, Xu J-W, Lai W-Y, et al. 5-methylcytosine promotes mRNA export—NSUN2 as the methyltransferase and ALYREF as an m5C reader. Cell Res. 2017;27:606–25.
29. Barbieri I, Kouzarides T. Role of RNA modifications in cancer. Nat Rev Cancer. 2020;20:303–22.
30. Liu J, Huang T, Chen W, Ding C, Zhao T, Zhao X, et al. Developmental mRNA m(5)C landscape and regulatory innovations of massive m(5)C modification of maternal mRNAs in animals. Nat Commun. 2022;13:2484.
31. Huang T, Chen W, Liu J, Gu N, Zhang R. Genome-wide identification of mRNA 5-methylcytosine in mammals. Nat Struct Mol Biol. 2019;26:380–8.
32. Selmi T, Hussain S, Dietmann S, Heiß M, Borland K, Flad S, et al. Sequence- and structure-specific cytosine-5 mRNA methylation by NSUN6. Nucleic Acids Res. 2021;49:1006–22.
33. Gu XR, Gustafsson C, Ku J, Yu M, Santi DV. Identification of the 16S rRNA m5C967 methyltransferase from *Escherichia coli*. Biochemistry. 1999;38:4053–7.
34. Tscherne JS, Nurse K, Popienick P, Michel H, Sochacki M, Ofengand J. Purification, cloning, and characterization of the 16S RNA m5C967 methyltransferase from *Escherichia coli*. Biochemistry. 1999;38:1884–92.
35. Blanco S, Dietmann S, Flores JV, Hussain S, Kutter C, Humphreys P, et al. Aberrant methylation of tRNAs links cellular stress to neuro-developmental disorders. EMBO J. 2014;33:2020–39.
36. Blanco S, Kurowski A, Nichols J, Watt FM, Benitah SA, Frye M. The RNA-methyltransferase Misu (NSun2) poises epidermal stem cells to differentiate. PLoS Genet. 2011;7:e1002403.
37. Frye M, Watt FM. The RNA methyltransferase Misu (NSun2) mediates Myc-induced proliferation and is upregulated in tumors. Curr Biol. 2006;16:971–81.
38. Gkatza NA, Castro C, Harvey RF, Heiß M, Popis MC, Blanco S, et al. Cytosine-5 RNA methylation links protein synthesis to cell metabolism. PLoS Biol. 2019;17:e3000297.
39. Edelheit S, Schwartz S, Mumbach MR, Wurtzel O, Sorek R. Transcriptome-wide mapping of 5-methylcytidine RNA modifications in bacteria, archaea, and yeast reveals m5C within archaeal mRNAs. PLoS Genet. 2013;9:e1003602.
40. Frommer M, McDonald LE, Millar DS, Collis CM, Watt F, Grigg GW, et al. A genomic sequencing protocol that yields a positive display of 5-methylcytosine residues in individual DNA strands. Proc Natl Acad Sci USA. 1992;89:1827–31.
41. Hussain S, Sajini AA, Blanco S, Dietmann S, Lombard P, Sugimoto Y, et al. NSun2-mediated cytosine-5 methylation of vault noncoding RNA determines its processing into regulatory small RNAs. Cell Rep. 2013;4:255–61.
42. Khoddami V, Cairns BR. Identification of direct targets and modified bases of RNA cytosine methyltransferases. Nat Biotechnol. 2013;31:458–64.
43. Schaefer M, Pollex T, Hanna K, Lyko F. RNA cytosine methylation analysis by bisulfite sequencing. Nucleic Acids Res. 2009;37:e12.
44. Wang Y, Zhao Y, Bollas A, Wang Y, Au KF. Nanopore sequencing technology, bioinformatics and applications. Nat Biotechnol. 2021;39:1348–65.
45. Hu Y, Chen C, Tong X, Chen S, Hu X, Pan B, et al. NSUN2 modified by SUMO-2/3 promotes gastric cancer progression and regulates mRNA m5C methylation. Cell Death Dis. 2021;12:842.
46. Song D, An K, Zhai W, Feng L, Xu Y, Sun R, et al. NSUN2-mediated mRNA m(5)C modification regulates the progression of hepatocellular carcinoma. Genom Proteom Bioinform. 2022;21:823–833.
47. Su J, Wu G, Ye Y, Zhang J, Zeng L, Huang X, et al. NSUN2-mediated RNA 5-methylcytosine promotes esophageal squamous cell carcinoma progression via LIN28B-dependent GRB2 mRNA stabilization. Oncogene. 2021;40:5814–28.
48. Wang L, Zhang J, Su Y, Maimaitiyiming Y, Yang S, Shen Z, et al. Distinct roles of m(5)C RNA methyltransferase NSUN2 in major gynecologic cancers. Front Oncol. 2022;12:786266.
49. Wang N, R-x Chen, M-h Deng, W-s Wei, Z-h Zhou, Ning K, et al. m5C-dependent cross-regulation between nuclear reader ALYREF and writer NSUN2 promotes urothelial bladder cancer malignancy through facilitating RABL6/TK1 mRNAs splicing and stabilization. Cell Death Dis. 2023;14:139.
50. Hall AE, Pohl SÖ-G, Cammareri P, Aitken S, Younger NT, Raponi M, et al. RNA splicing is a key mediator of tumour cell plasticity and a therapeutic vulnerability in colorectal cancer. Nat Commun. 2022;13:2791.
51. Merlos-Suárez A, Barriga FM, Jung P, Iglesias M, Céspedes MV, Rossell D, et al. The intestinal stem cell signature identifies colorectal cancer stem cells and predicts disease relapse. Cell Stem Cell. 2011;8:511–24.
52. Gudiño V, Pohl S, Billard CV, Cammareri P, Bolado A, Aitken S, et al. RAC1B modulates intestinal tumourigenesis via modulation of WNT and EGFR signalling pathways. Nat Commun. 2021;12:2335.

53. Anoopkumar-Dukie S, Carey JB, Conere T, O'Sullivan E, van Pelt FN, Allshire A. Resazurin assay of radiation response in cultured cells. Br J Radio. 2005;78:945–7.
54. Shibata H, Toyama K, Shioya H, Ito M, Hirota M, Hasegawa S, et al. Rapid colorectal adenoma formation initiated by conditional targeting of the Apc gene. Science. 1997;278:120–3.
55. Faller WJ, Jackson TJ, Knight JRP, Ridgway RA, Jamieson T, Karim SA, et al. mTORC1-mediated translational elongation limits intestinal tumour initiation and growth. Nature. 2015;517:497–500.
56. Crooks GE, Hon G, Chandonia JM, Brenner SE. WebLogo: a sequence logo generator. Genome Res. 2004;14:1188–90.
57. Chen SY, Chen KL, Ding LY, Yu CH, Wu HY, Chou YY, et al. RNA bisulfite sequencing reveals NSUN2-mediated suppression of epithelial differentiation in pancreatic cancer. Oncogene. 2022;41:3162–76.
58. Amleh A, Nair SJ, Sun J, Sutherland A, Hasty P, Li R. Mouse cofactor of BRCA1 (Cobra1) is required for early embryogenesis. PLoS One. 2009;4:e5034.
59. Cai J, Maitra A, Anders RA, Taketo MM, Pan D. β-Catenin destruction complex-independent regulation of Hippo-YAP signaling by APC in intestinal tumorigenesis. Genes Dev. 2015;29:1493–506.
60. Gregorieff A, Liu Y, Inanlou MR, Khomchuk Y, Wrana JL. Yap-dependent reprogramming of Lgr5(+) stem cells drives intestinal regeneration and cancer. Nature. 2015;526:715–8.
61. Schwitalla S, Fingerle AA, Cammareri P, Nebelsiek T, Göktuna SI, Ziegler PK, et al. Intestinal tumorigenesis initiated by dedifferentiation and acquisition of stem-cell-like properties. Cell. 2013;152:25–38.
62. Luo G, Xu W, Chen X, Wang S, Wang J, Dong F, et al. NSUN2-mediated RNA m(5)C modification modulates uveal melanoma cell proliferation and migration. Epigenetics. 2022;17:922–33.
63. Blanco S, Bandiera R, Popis M, Hussain S, Lombard P, Aleksic J, et al. Stem cell function and stress response are controlled by protein synthesis. Nature. 2016;534:335–40.
64. Lin Y, Zhao Z, Nie W, Huang M, Cai J, Wang Y, et al. Overview of distinct 5-methylcytosine profiles of messenger RNA in normal and knock-down NSUN2 colorectal cancer cells. Front Genet. 2023;14:1121063.
65. Dominissini D, Nachtergaele S, Moshitch-Moshkovitz S, Peer E, Kol N, Ben-Haim MS, et al. The dynamic N1-methyladenosine methylome in eukaryotic messenger RNA. Nature. 2016;530:441–6.
66. Rieder D, Amort T, Kugler E, Lusser A, Trajanoski Z. meRanTK: methylated RNA analysis ToolKit. Bioinformatics. 2016;32:782–5.
67. Legrand C, Tuorto F, Hartmann M, Liebers R, Jacob D, Helm M, et al. Statistically robust methylation calling for whole-transcriptome bisulfite sequencing reveals distinct methylation patterns for mouse RNAs. Genome Res. 2017;27:1589–96.
68. Konno M, Koseki J, Asai A, Yamagata A, Shimamura T, Motooka D, et al. Distinct methylation levels of mature microRNAs in gastrointestinal cancers. Nat Commun. 2019;10:3888.
69. Goldman MJ, Craft B, Hastie M, Repečka K, McDade F, Kamath A, et al. Visualizing and interpreting cancer genomics data via the Xena platform. Nat Biotechnol. 2020;38:675–8.
70. Tang D, Chen M, Huang X, Zhang G, Zeng L, Zhang G, et al. SRplot: A free online platform for data visualization and graphing. PLoS ONE. 2023;18:e0294236.

ACKNOWLEDGEMENTS

This study is generously funded by the Republic of Türkiye, Ministry of National Education, Selection and Placement of Candidates Sent Abroad for Postgraduate Education (YLSY) scholarship programme. This work was also funded by Cancer Research UK (CRUK) under Career Development Fellowship, A19166 (K.B.M.), the European Research Council under Starting Grant, COLGENES-715782 (K.B.M.), and the MRC under Project Grant MR/X008762/1 (K.B.M.). We thank Prof Andrew Jackson (IGC) for support with *Lgr5* RNAscope. We thank all the member of the Myant lab for their support during the progression of this project. We are grateful to collaborate with Szu-Ying Chen, who received a student scholarship from NSTC#A1102-U015 and NCKU-SP112002, and Professor Po-Hsien Huang in Taiwan.

AUTHOR CONTRIBUTIONS

ABA conceived the research and most of the experiments. CVB produced the virus required for knockdown experiments and histology sections. CVB, PC and SÖP contributed to the experiments. Preliminary RNA-seq data obtained from AH and PP. SYC analysed mRNA-Bisulfite sequencing. VR carried out the Lgr5 RNAscope. KBM, FVND, PHH, MGD and SF provided critical advice. ABA and KBM wrote the manuscript with contributions from all other authors.

COMPETING INTERESTS

The authors declare no competing interests.

ADDITIONAL INFORMATION

Supplementary information The online version contains supplementary material available at https://doi.org/10.1038/s41419-026-08560-0.

Correspondence and requests for materials should be addressed to Kevin B. Myant.

Reprints and permission information is available at http://www.nature.com/reprints

Publisher's note Springer Nature remains neutral with regard to jurisdictional claims in published maps and institutional affiliations.